3D controlled-source electromagnetic imaging of gas hydrates: Insights from the Pelotas Basin offshore Brazil

Raghava Tharimela[1], Adolpho Augustin[2], Marcelo Ketzer[3], Jose Cupertino[2], Dennis Miller[4], Adriano Viana[5], and Kim Senger[6]

Abstract

Mapping of natural gas hydrate systems has been performed successfully in the past using the controlled-source electromagnetic (CSEM) method. This method relies on differentiating resistive highly saturated free gas or hydrate-bearing host sediment from a less resistive low-saturated gas or brine-bearing host sediments. Knowledge of the lateral extent and resistivity variations (and hence the saturation variations) within sediments that host hydrates is crucial to be able to accurately quantify the presence of saturated gas hydrates. A 3D CSEM survey (PUCRS14) was acquired in 2014 in the Pelotas Basin offshore Brazil, with hydrate resistivity mapping as the main objective. The survey was acquired within the context of the CONEGAS research project, which investigated the origin and distribution of gas hydrate deposits in the Pelotas Basin. We have inverted the acquired data using a proprietary 3D CSEM anisotropic inversion algorithm. Inversion was purely CSEM data driven, and we did not include any a priori information in the process. Prior to CSEM, interpretation of near-surface geophysical data including 2D seismic, sub-bottom profiler, and multibeam bathymetry data indicated possible presence of gas hydrates within features identified such as faults, chimneys, and seeps leading to pockmarks, along the bottom simulating reflector and within the gas hydrate stability zone. Upon integration of the same with CSEM-derived resistivity volume, the interpretation revealed excellent spatial correlation with many of these features. The interpretation further revealed new features with possible hydrate presence, which were previously overlooked due to a lack of a clear seismic and/or multibeam backscatter signature. In addition, features that were previously mapped as gas hydrate bearing had to be reinterpreted as residual or low-saturated gas/hydrate features, due to the lack of significant resistivity response associated with them. Furthermore, we used the inverted resistivity volume to derive the saturation volume of the subsurface using Archie's equation.

Introduction

Natural gas hydrates are found globally in marine and onshore environments in which natural gas migrates through zones with suitable pressure-temperature and reservoir conditions (Kvenvolden, 1993; Sloan and Koh, 2007; Pinero et al., 2013). Gas hydrates potentially host significant volumes of methane that represent

1) a potential energy resource (Collett et al., 2009; Boswell and Collett, 2011)
2) a possible climate forcer should methane from hydrate deposits be released to the atmosphere (Kennett et al., 2003; Dickens, 2011; Hunter et al., 2013)
3) a hazard with impacts for hydrocarbon drilling and production operations (Grauls, 2001; Freij-Ayoub et al., 2007; McConnell et al., 2012).

Hydrate mapping traditionally relies on seismic methods (bottom simulating reflector or "BSR," e.g., Hyndman and Spence, 1992) and sparse well data. These relate to mapping the contrasts setup by the overlying high-velocity hydrate with the low-velocity free gas trapped beneath it. However, the challenge is to adequately characterize and quantify the extent and saturation of hydrate-bound and hydrate-associated gas. This is difficult to attain with seismic data alone, given

[1]Electromagnetic Geoservices Asia Pacific, 7th floor East Wing, Rohas PureCircle, No. 9 Jalan P. Ramlee, Kuala Lumpur 50250, Malaysia. E-mail: rtharimela@emgs.com.
[2]Pontifícia Universidade Católica do Rio Grande do Sul, Instituto do Petróleo e dos Recursos Naturais, Av. Ipiranga 6681, Porto Alegre 90619-900, Brazil. E-mail: adolpho.augustin@pucrs.br; jose.cupertino@pucrs.br.
[3]Linnaeus University, Department of Biology and Environmental Science, Kalmar 39131, Sweden. E-mail: marcelo.ketzer@lnu.se.
[4]PETROBRAS — CENPES Centro de Pesquisas e Desenvolvimento Leopoldo Américo Miguez de Mello, Rio de Janeiro 21941-915, RJ, Brazil. E-mail: miller@petrobras.com.br.
[5]PETROBRAS — E&P EXPLORATION, Rio de Janeiro 20031-170, RJ, Brazil. E-mail: aviana@petrobras.com.br.
[6]University Centre in Svalbard, Department of Arctic Geology, PO Box 156, 9171 Longyearbyen, Norway. E-mail: kim.senger@unis.no.

Manuscript received by the Editor 16 November 2018; revised manuscript received 5 July 2019; published ahead of production 23 August 2019; published online 14 October 2019. This paper appears in *Interpretation*, Vol. 7, No. 4 (November 2019); p. SH111–SH131, 20 FIGS., 2 TABLES.
http://dx.doi.org/10.1190/INT-2018-0212.1.

the limited difference between acoustic velocities in low- and high-saturation deposits (Constable, 2010; Hesthammer et al., 2010). On the other hand, resistivity information is routinely used to estimate gas saturation through Archie's original equation (Archie, 1942) or various subsequent improvements of this empirical method (e.g., Worthington, 1993; Cook and Waite, 2018). Significant changes in resistivity are not obtained until the pore fluid is dominantly gas (Constable, 2010) with the resistivity primarily controlled by the presence and connectivity of electrically conductive brine (Senger et al., 2017). This is also true for gas hydrates, based on the laboratory studies. Pure hydrate is highly resistive (e.g., Du Frane et al., 2011), but the saturation and connectivity of solid gas hydrate within the gas hydrate-bearing strata determine the overall formation resistivity (Spangenberg and Kulenkampff, 2006; Du Frane et al., 2015).

Controlled-source electromagnetic (CSEM) is a powerful technique to quantify subsurface resistivity remotely, prior to drilling (e.g., Constable, 2010; MacGregor and Tomlinson, 2014). The 3D CSEM acquisition and inversion for conventional hydrocarbon accumulations has been proven to be effective at deep (1000–4000 m) and shallow burial depths (from the seafloor up to 1000 m), and it is routinely applied in shallow and deepwater settings. Due to a combination of factors such as the lower operational frequency range (from 0.05 to 50 Hz) and guided wave principle, the vertical resolution is inferior. Spatially, however, the lateral extent of the resistive body can be well-constrained by 3D CSEM provided that an appropriate grid geometry and survey parameters such as waveform and source power are applied (Fanavoll et al., 2014; Granli et al., 2017). CSEM data can be acquired using a range of acquisition setups typically combining a towed source with receivers deployed either as seafloor nodes or using a towed streamer (MacGregor and Tomlinson, 2014; Constable et al., 2016), with implications on data quality, data sampling, and efficiency and cost of the acquisition. The commercial success of CSEM since its establishment in the early 2000s (e.g., Eidesmo et al., 2002; Edwards, 2005) builds upon early academic success focusing on mapping shallow resistors in deepwater settings. As such, gas hydrates are considered an optimal CSEM target, and a number 2D CSEM campaigns conducted by university groups have been acquired in the past, including surveys of the Cascadia margin offshore Oregon (Weitemeyer et al., 2006, 2011) and Vancouver Island (Gehrmann et al., 2016), mid-Norway (Attias et al., 2016), west Svalbard margin (Goswami et al., 2015, 2017), New Zealand (Schwalenberg et al., 2010a, 2010b, 2017), and the Gulf of Mexico (Weitemeyer and Constable, 2010). All of the gas hydrate CSEM surveys published so far indicate the presence of hydrates but lack information about their areal extent. To obtain a comprehensive spatial distribution, it is extremely important to use 3D against a 2D acquisition where possible. To the best of our knowledge, no results of 3D inversion of a 3D CSEM hydrate-specific survey has been reported in the scientific literature, although a few hydrate specific 3D campaigns have been acquired in the Gulf of Mexico (Weitemeyer and Constable, 2010; Kannberg and Constable, 2017) and offshore Japan (OEdigital, 2014).

Here, we present the results of a 3D CSEM survey targeted specifically to delineate gas hydrates in the Pelotas Basin offshore Brazil. The main objectives of this paper are to

1) Provide an overview of a gas hydrate specific 3D CSEM acquisition setup used for this survey.
2) Describe the quality of the acquired data, the processing, quality-control, and inversion processes.
3) Jointly interpret the 3D CSEM results with near-surface observations from the multibeam backscatter data and 2D seismic, mainly focusing within the gas hydrate stability zone.

Geological settings

The Pelotas Basin is a passive margin basin formed during the rifting of the Gondwana supercontinent and drifting of the South Atlantic (Asmus and Baisch, 1983) (Figure 1). It is limited to the north by the Santos Basin by the Florianopolis High and to the south by the Punta del Este Basin by the Cabo Polonio High. The most important physiographic feature of the Pelotas Basin is the Rio Grande Cone (RGC) (Martins et al., 1972). The RGC consists of a protuberance in the continental slope, and it is the main depocenter of the basin with an accumulation of ≈ 7 km of sediments from the Barremian to Recent (Saunders et al., 2013). The RGC is experiencing a gravitational collapse in which a major detachment fault occurs at the base of the Lower Miocene. The main structures associated with the detachment system are normal faults in a proximal extensional domain and folds and thrust imbricates in a distal compressional domain (Silveira and Machado, 2004; Castillo et al., 2009; Figure 1). Faults related to the gravitational collapse of the RGC are probable migration pathways for the shallow gas in the basin (Oliveira et al., 2010; Miller et al., 2015). Gas anomalies at shallow depths below the seafloor (<10 m) underneath pockmarks have been identified in mud gas analyses from piston cores and high-resolution acoustic data (3.5 kHz; Rodrigues et al., 2017).

The occurrence of gas hydrates has been indicated by the presence of BSRs in an area of 45,000 km^2 within water depths of 500–3500 m and at approximately 400 m below the seafloor in the study area (Fontana, 1989; Fontana and Mussumeci, 1994; Sad et al., 1997, 1998). The average thickness of the hydrate stability zone (the distance between the seafloor and the BSR) is approximately 450 m in the entire RGC and thins abruptly to zero at 500 m of water depth (Miller et al., 2015), which coincides with the depth of the edge of the hydrate sta-

bility zone calculated for the area using water temperature profiles (Ketzer et al., 2019). Gas hydrate samples were only obtained in piston cores within pockmarks, with the shallowest hydrate recovery at 1.4 m below the seafloor (Miller et al., 2015). Low chlorine concentration anomalies are interpreted as being related to hydrate disassociation during piston core recovery. Sad et al. (1998) estimate that the hydrates in the Pelotas Basin contain as much as 780 trillion cubic feet of gas. More recent studies based on the reprocessing of seismic data (time frequency decomposition) pointed to the existence of spectral anomalies that could be possibly related to gas reservoirs that are a source of hydrates, free gas accumulations underneath the BSR, the presence of the hydrates itself, and to gas flux along gas chimneys (Oliveira et al., 2010).

Two pockmark fields have been mapped in the RGC using a multibeam echo sounder. The first one is restricted to water depths between 500 and 600 m (Miller et al., 2015). The second pockmark field is located at water depths between 1000 and 2000 m, where the CSEM survey was performed. Pockmarks in this field occur in an area of 8 × 40 km and follow a northwest–southeast trend, oblique to the regional bathymetry and following a series of outcropping valley-forming faults (Miller et al., 2015; Figure 2). The density of pockmarks in this field is <1 per km^2, diameters of individual pockmarks range from 300 to 1200 m, and depths vary from 4 to 13 m (Miller et al., 2015). Chemosynthesis-based communities have been identified and described in one of the pockmarks (Giongo et al., 2016; Medina-Silva et al., 2017). Patches of high-backscatter anomalies may also indicate their occurrence in adjacent pockmarks, along with possible shallow gas hydrates and carbonates related to the anaerobic oxidation of methane (Miller et al., 2015). Gas hydrate samples have been obtained from piston cores collected inside pockmarks in both areas, and analyses of dissociated gas indicated (1) a dominantly methane composition (>99 vol%) and (2) a biogenic origin based on the stable carbon isotopic composition of methane (−66.7 to −69.3‰; Miller et al., 2015).

CSEM sensitivity assessment

Prior to data acquisition, CSEM sensitivity assessment is performed to evaluate the minimum target dimensions/properties that CSEM is capable of detecting in the study area.

CSEM sensitivity depends primarily on the target burial depth, areal extent, thickness, and resistivity contrast of the target with the surrounding background resistivity. A synthetic CSEM response of a nonhydrate background model and hydrate bearing target model (with specific target properties) is simulated during this assessment process. The sensitivity is then defined as the difference between the target synthetic response and the background synthetic response normalized against the uncertainty (Mittet and Morten, 2012). If the difference between the target and background response is significantly larger than the uncertainty (>3 times), there is a high probability that CSEM can detect the target. Conversely if the contrast is small compared with the uncertainty (i.e., 1–3 times) then the target would be considered to have a low probability of detection. A target response of less than 1 would mean that

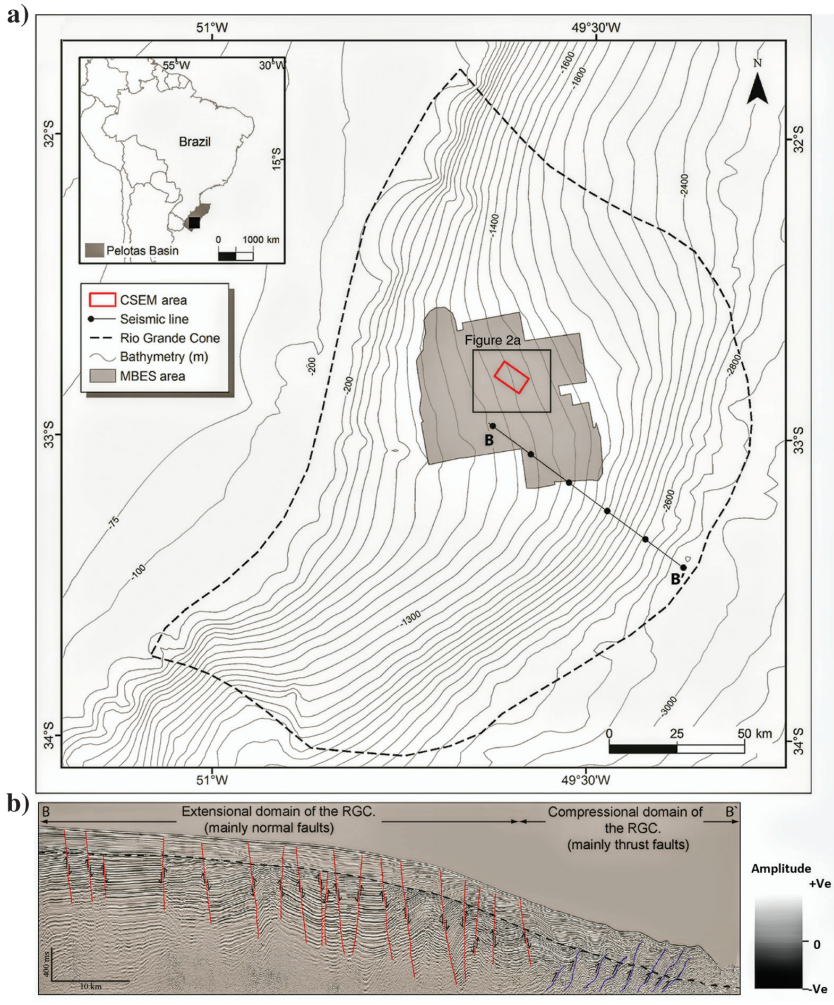

Figure 1. (a) Location map of the study area in the Pelotas Basin showing the location of the CSEM survey area in the red rectangle and the multibeam echosounder area in the gray polygon. (b) Regional seismic section showing the main structures of the RGC: normal faults (the red lines) in a proximal extensional domain, and folds and thrust imbricates (the blue lines) in a distal compressional domain. Note the BSR (the dashed line) in the seismic section indicating the base of the gas hydrate stability zone (modified from Miller et al., 2015).

uncertainty dominates the signal; hence, the target is not detectable.

A simple 3D modeling exercise can be performed by constructing a 1D plain layer background resistivity model with water depth and subsurface layer thickness and corresponding resistivities as input. A target model is built by including a "pizza-box" shaped 3D target within the background model at a known target depth. The sensitivity evaluated is based on the peak target response from a single receiver, which is positioned at an optimum location to detect the target. The runtime for this type of modeling is in minutes, and one can achieve a representative target sensitivity estimate using this method. This type of modeling does not take into account the structural and geometric variation in the subsurface and target. A full-scale 3D modeling exercise (as shown in Appendix A) can be performed using seismic horizons and target polygons as input for background and target model building. This type of modeling provides a more realistic sensitivity assessment. One can also perform grid design tests for an optimum grid design assessment. The runtime for this exercise is from a week to a month based on the size of the input model(s) and designed survey grid(s).

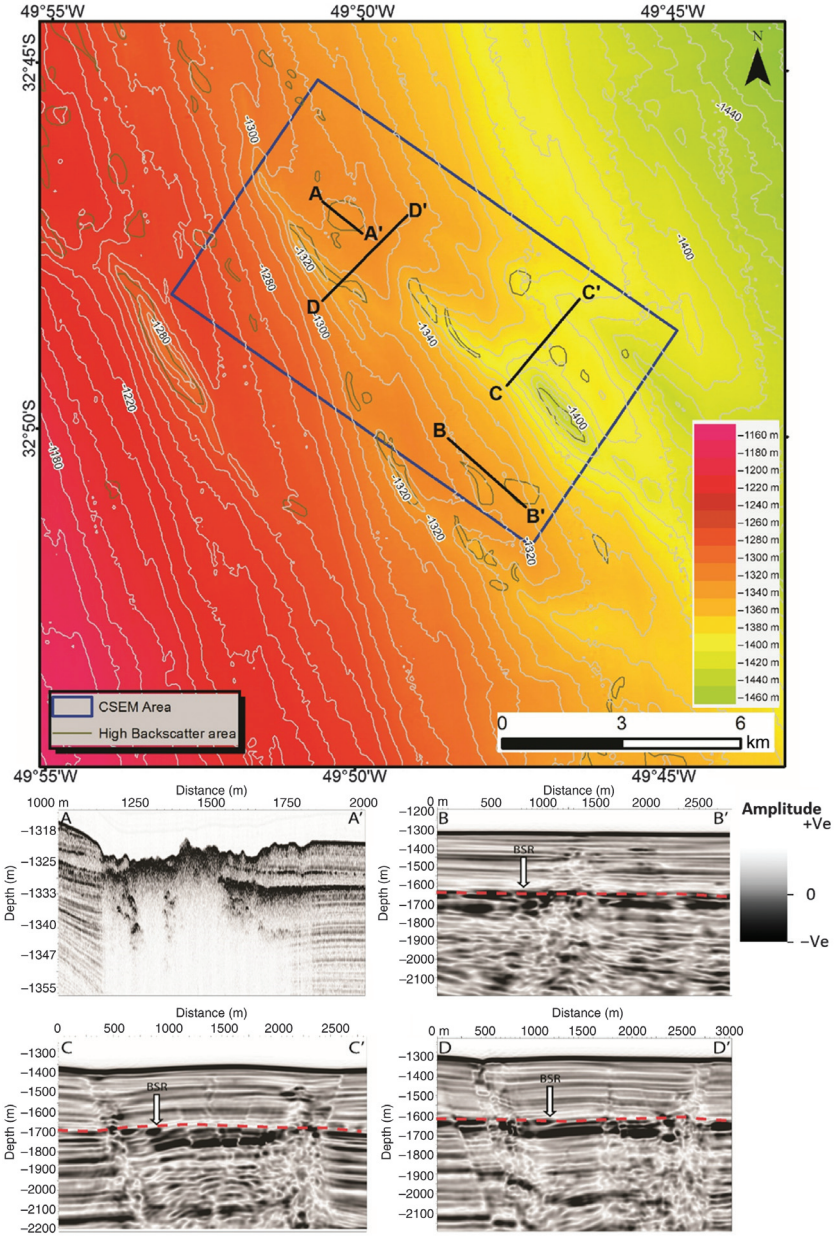

Figure 2. Detailed bathymetric map of the northeast portion of the RGC showing the study area (the blue rectangle). Note the presence of backscatter anomalies associated with pockmarks (the brown polygons) and the orientation of pockmarks following the northwest–southeast trend of outcropping valley-forming faults (modified from Miller et al., 2015). A-A′ is the trace of a high-resolution (3.5 kHz) sub-bottom profiler section showing acoustic blankings related to gas flow below a pockmark (A; modified from Miller et al., 2015); B-B′, C-C′, and D-D′ are the traces of seismic sections crossing a set of normal faults of the extensional domain in the study area (B, C, and D). Note the presence of a strong amplitude anomaly below the BSR. These seismic lines are used in Figure 13 for the superimposition of acoustic and CSEM data.

Presurvey sensitivity assessment for this project was done using simple 3D modeling. A plain layer background model was constructed, and a target (i.e., the hydrate in this case) is included immediately below the seafloor (Figure 3a). The target thickness is varied between 5 and 200 m, and the target is assumed to be a rectangular box with an area ranging between 0.1 and 1 km^2. A scan of sensitivity points for targets of a range of thickness and area combinations (within the target thickness and area limits set) is plotted in a thickness versus area crossplot (Figure 3b). In the plot, all of the thickness and area combinations that fall within the red are considered below CSEM sensitivity, those in yellow have marginal CSEM sensitivity, and data points that fall within the green have high CSEM sensitivity.

Frequencies and source-receiver offsets that would be sensitive to this shallow buried target can be seen in the frequency versus offset crossplot shown in Figure 3c. Frequencies ranging between 1 and 20 Hz and offsets in the range of approximately 1000–4000 m source receiver offset would be needed for hydrate detection. The source waveform to be used for the survey is designed based on this presurvey sensitivity study assessment.

CSEM data acquisition

The PUCRS14 survey was acquired using a vessel called the *EM Leader*.

The water depth in the survey area varies from 1250 to 1400 m, and the area contained several pockmarks in which shallow (~2 m below seafloor) gas hydrates have been recovered (Miller et al., 2015). The CSEM survey acquisition time was 15 days.

An appropriate grid design is important to image the target accurately. The grid design depends primarily on the target burial depth and target size. An inversion is more likely able to reconstruct a target if the target information is recorded by multiple receivers in that grid. If the target is small or at the edge/outside the receiver grid and its information is recorded only by one or two receivers, the inversion would have limited data points and is less likely to reconstruct the target. In terms of grid spacing for a shallow buried target, Granli et al. (2017) discuss how a combination of denser grid and high-frequency waveform is necessary to achieve higher resolution CSEM result. Synthetic inversion studies conducted over a combination of grids (Appendix A) suggest that a denser grid design is necessary to image thin and elongated targets such as chimneys and faults. Two sets of source tow configurations were tested, one towing over the receiver line and the second towing at a 250 m offset from the receiver lines (i.e., towing in between receiver lines that are spaced 500 m apart). For the case in which the source is towed along the receiver lines and the receivers record a very strong EM signal when the source is passing directly above a receiver at zero offset. This leads to very high sensitivity directly beneath the receiver, and inversion tends to update these model cells to unrealistic resistivity values causing inversion artifacts also known as "acquisition footprints." This can be mitigated by applying a smoothness regularization in the inversion, a practice commonly used in traditional hydrocarbon exploration in which the target is deep. But in the case of shallow targets such as hydrates, this smoothness regularization would impact the near-surface imaging through unwanted smoothing. When the source is towed slightly away from the receivers, these footprints are reduced considerably and one can achieve a less artifact-prone image of the subsurface. Thus, the latter design was considered for this survey.

Acquisition was conducted using a dense 3D survey grid configuration with 132 multicomponent receivers deployed on the seabed, measuring the horizontal electric field E and magnetic field H, along 12 receiver lines (Figure 4). The receiver spacing is 1000 m along the source tow direction and 500 m across the source tow direction. A 280 m long deep towed horizontal electric dipole source with 1250 A output current was used for surveying. This is a standard source setup primarily used for conventional hydrocarbon exploration. A shorter dipole could improve the resolution; however, synthetic studies (Appendix A) suggest that the setup used for this survey provides sufficient resolution to image the target that falls within CSEM sensitivity limits. The source was towed 13 times along northwest–southeast oriented profiles, at approximately 30 m altitude from the seafloor (01Tx001–01Tx13; Figure 4). Additional towing perpendicular to the receiver lines with evenly spaced towlines could provide more surface data samples thus leading to better resolution; however, this was not considered in this survey due to cost constraints. Instead, a dense cross-receiver line spacing (i.e., dense spacing between receiver lines) with the

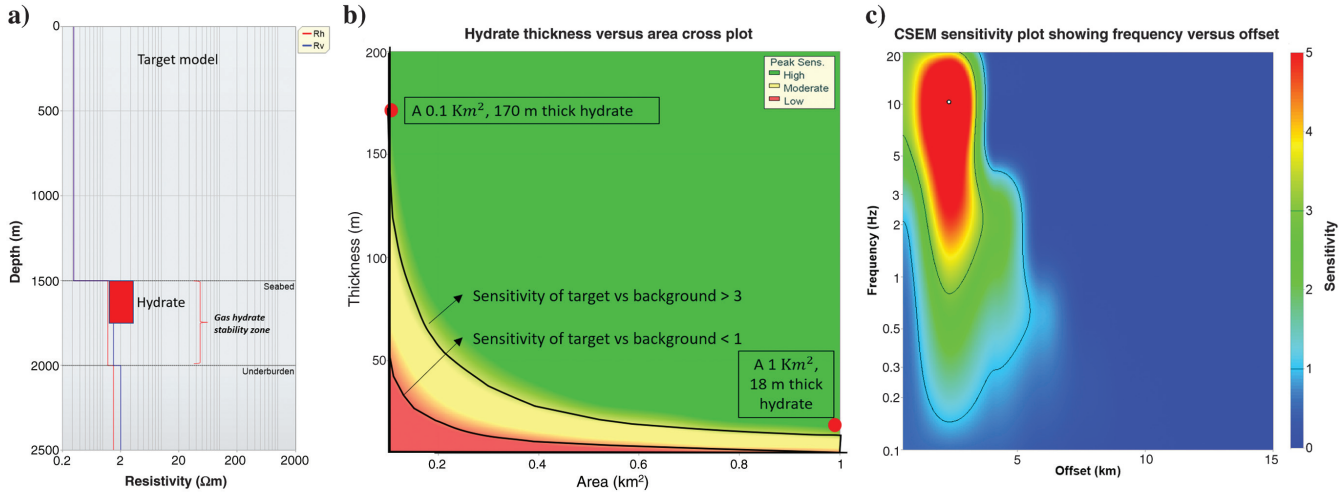

Figure 3. The CSEM presurvey sensitivity assessment. (a) The 1D background model with 3D target hydrate. (b) Thickness versus area crossplot indicating a CSEM sensitivity scan for various combinations of thickness and area. If the hydrate target with a combination of area and thickness falls in the green region (i.e., sensitivity of the target versus background >3), it has a high CSEM sensitivity; if it falls in the yellow region (i.e., sensitivity of the target versus background between 3 and 1), it will have moderate sensitivity; and if it falls in the red region (i.e., sensitivity of the target versus background <1), then it will have low CSEM sensitivity. Two possible thickness versus area combinations of hydrate that CSEM would be sensitive to are indicated. (c) The frequency and offset that would be sensitive to a given hydrate target are shown in the frequency versus offset crossplot. The red region indicates high sensitivity, and the blue region indicates low/no sensitivity. This plot suggests that the main frequencies detecting hydrates range between 1 and 19 Hz in source receiver offsets ranging between 500 and 3000 m.

source being towed in between the receiver lines was chosen to achieve a dense and uniform illumination of the shallow subsurface. All of the receivers were deployed on the seafloor prior to source tow providing a full 3D azimuthal data coverage. With the input from a presurvey sensitivity study, a composite source waveform with a base frequency of 1 Hz was used in this survey. Figure 5 shows the waveform in the time and frequency domains. Eight frequencies were processed (1, 3, 5, 7, 9, 11, 13, and 19 Hz).

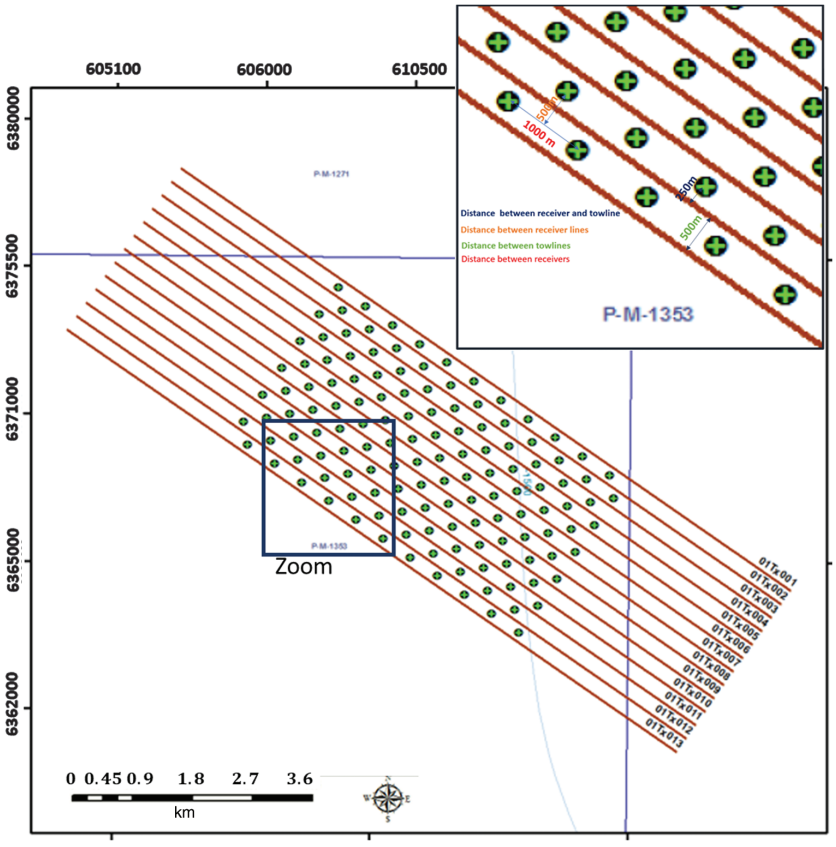

Figure 4. Survey layout designed to map gas hydrates. The magnified section on the right gives the details of the grid geometry. The black circles with green + indicate the receivers, and the brown lines indicate the source towlines. The data is acquired and plotted for all the plots in SIRGAS2000-UTM22S UTM zone.

CSEM data processing and 3D CSEM inversion

The acquired data were calibrated and demodulated as part of the offshore processing routine. The demodulated data were scaled to the source dipole moment. As a preparation for 3D inversion, the receiver data were rotated so that the inline components (x-component of the E channel and the y-component of the H channel) are aligned to the towline direction. We expect that one would achieve good inversion results even without the rotation step because the inversion code used here updates and further fine-tunes the rotation angles with every iteration (Morten and Bjørke, 2010). Finally, noisy data points are masked through a signal-to-noise ratio threshold. Figure 6a shows magnitude plots of the demodulated data for the Ex, Ey and Hx, Hy channels for the base frequency for a single receiver (01Rx060a). Figure 6b shows the final rotated masked data of the same receiver for the same frequency and same channels. Figure 6c and 6d shows

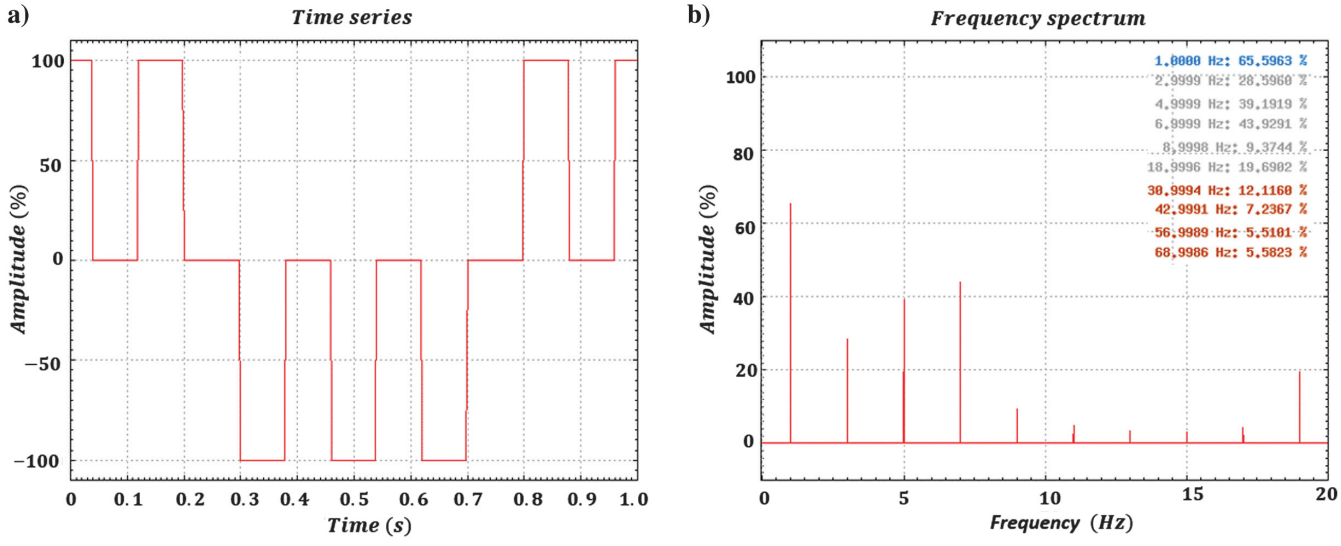

Figure 5. Composite source waveform transmitted by the source during the PUCRS14 acquisition. (a) Source signal amplitude in percentage represented in the time domain. (b) Source signal amplitude represented in percentage in the frequency domain. The percentage source current transmitted to different frequencies is shown in the top-right corner. This waveform is designed so that the highest energy is on 1 Hz, which is the base frequency.

the rotated masked magnitude and phase plots for the Ex and Hy channels for all the receivers along the towline (Tx005).

In general, the data are of very good quality for all of the processed frequencies as exemplified in Figure 7 for the magnetic x- and y-components for receiver 01Rx60a in the source-receiver offset domain. The first data sample was recorded at a 250 m source-receiver offset (shows as the magnified image in Figure 7) as the source was towed with an offset of 250 m from the receiver line. As per the pre-survey sensitivity recommendations, data samples up to a 6000 m source-receiver offset were processed. The noise floor for the electric E channel data is seen at $1e^{-16}$ V/Am^2, and the noise floor for the magnetic H data is seen at $\sim 1e^{-13}$ 1/m^2.

Data between the first sample and inner offset limit are not included in the inversion because these very short offsets primarily carry information about the seawater resistivity (direct wave) along with a small component of the signal from the subsurface. Because relative uncertainty is scaled against the total field, which is dominated by this strong direct wave component, the measurement uncertainty from this direct wave will exceed the subsurface signal in this very short offset data leading to a very small contribution from these offsets to the overall error function. The inner offset limit considered in this study might be conservative; however, synthetic inversion studies (Appendix A) demonstrate that these offsets have sufficient information about the target to be imaged.

Anisotropic 1D and 2.5D inversions were run on the processed data to delineate the general background resistivity trend in the area. The results indicated minor anisotropy in the subsurface with a vertical resistivity component varying between 1.3 and 1.5 Ωm and a horizontal resistivity component of approximately 1.2 Ωm. Some receivers indicated higher vertical resistivity, possibly due to their proximity to hydrates. The knowledge gathered from these inversions formed the basis for selecting resistivity values for the 3D inversion start model.

A purely CSEM data driven, anisotropic 3D inversion was run using a start model with a single value vertical resistivity of 1.4 Ωm and horizontal resistivity of 1.2 Ωm in the subsurface, without using any a priori information from seismic or well-log data except the bathymetry and water column resistivity (Figure 8). The water column resistivity profile was measured during CSEM data acquisition using a conductivity, temperature, density sensor probe connected to the source. Measurements are made while the source is being deployed and retrieved while towing along each line. For this survey, all of the measured profiles (along all of the lines) indicated a similar trend of water conductivity with no major variations. The average of all of the profiles providing conductivity information from sea level until 30 m above the water bottom in which the source is towed, was imprinted in the water column of the start model. A cubic cell geometry ($X = 40$ m, $Y = 40$ m, and $Z = 40$ m) was selected to obtain a

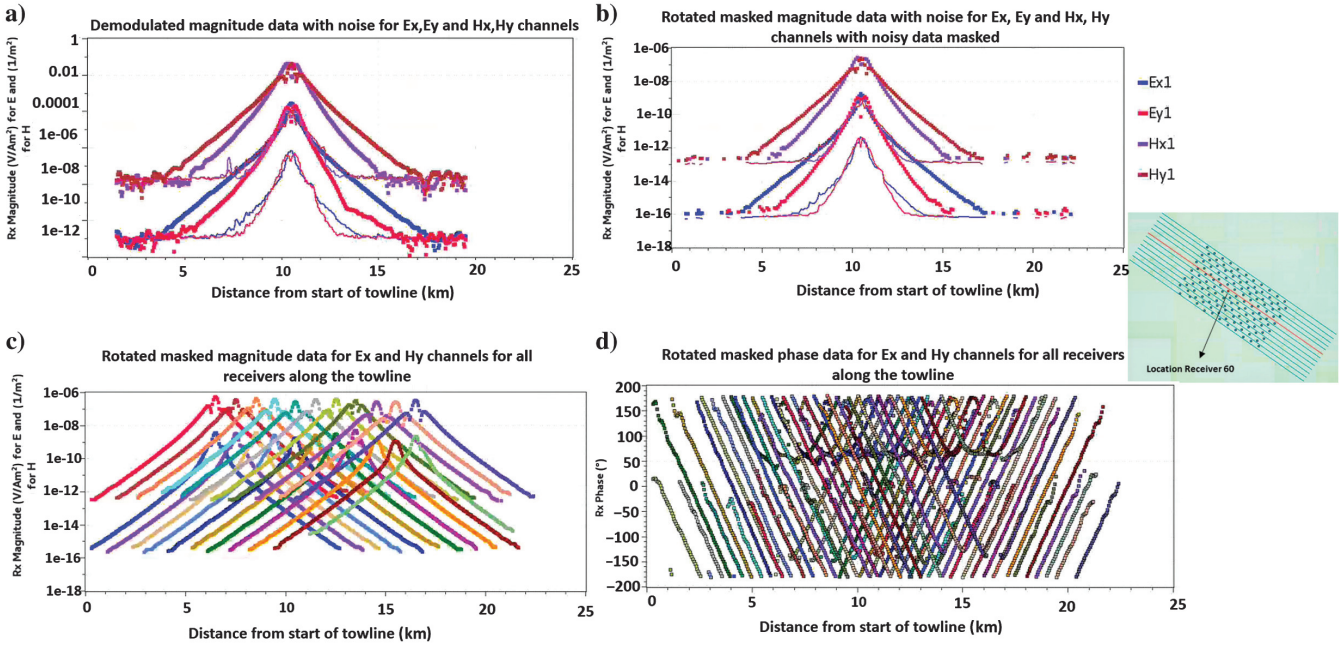

Figure 6. The CSEM data processing example shown for receiver 01Rx60a along towline Tx005 for the base frequency (1 Hz). (a) Magnitude of receiver 01Rx60a plotted along the towline, showing the demodulated signal of all of the processed channels. (b) Magnitude of receiver 01Rx60a plotted along the towline, showing all of the channels after rotation and masking of noisy data. The colored squares indicate the signal of each channel, and the line indicates noise of the corresponding channel. (c) Plot showing magnitude for the Ex and Hy channels for all of the receivers along towline Tx005a. (d) Plot showing phase for the Ex and Hy channels for all of the receivers along towline Tx005a. Location of the receiver and the towline in the survey grid shown in the image on the right.

sufficiently fine inversion model grid. An even finer cell size could provide improved modeling accuracy especially at the seabed; however, this would increase the computation time by severalfold. To bypass this and to improve the modeling accuracy, the modeling code in the inversion is enabled to upscale the bathymetry of the input model to a smooth fine-scale grid in the forward-modeling stage (Shantsev and Maao, 2014). The inversion algorithm is a gradient-based Broyden-Fletcher-Goldfarb-Shanno (Zhu et al., 1997; Zach et al., 2008) algorithm, which iteratively updates the subsurface resistivity until a model is found that explains the measured data to within the data uncertainty. A full-azimuth 3D CSEM data provide good sensitivity to the vertical resistivity Rv component and the horizontal resistivity Rh component of subsurface (Morten and Bjørk, 2010).

Data were inverted using the electric (Ex, Ey) and magnetic (Hx, Hy) channels separately. The quality of the final inversion is assessed based on qualitative factors such as the geologic plausibility of the resultant model and quantitative factors such as the final data fit. As part of the geologic plausibility assessment, both inversions were compared with available 2D seismic (Figure 9). The inverted model from the electric channel inversion appears noisier compared to the inverted model from the magnetic channel. Some of the resistive anomalies seen on the electric channel-based inversion do not seem to match with seismic events and appeared

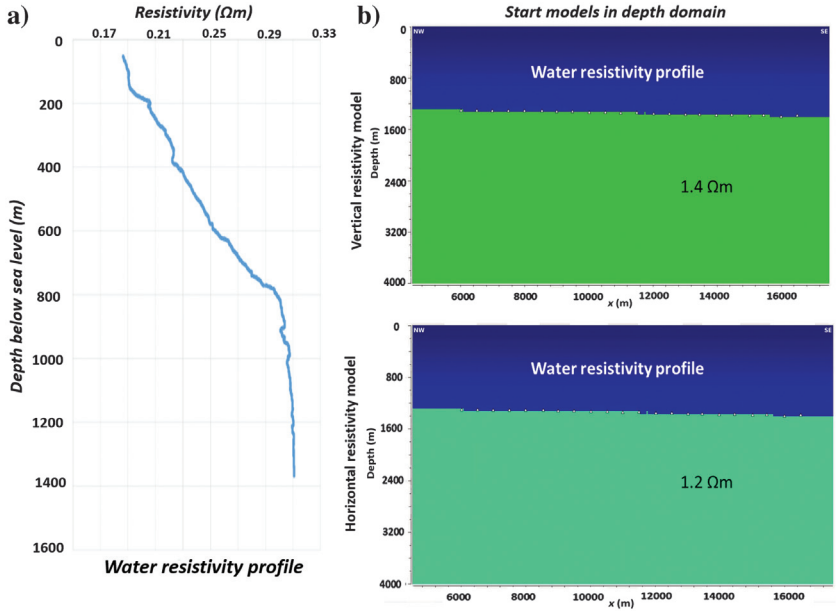

Figure 8. Start models used in the inversion. (a) Water resistivity profile imprinted in the water layer of the start model. (b) Start model vertical resistivity (top panel) and horizontal resistivity (bottom panel); cross sections shown along Tx005 towline.

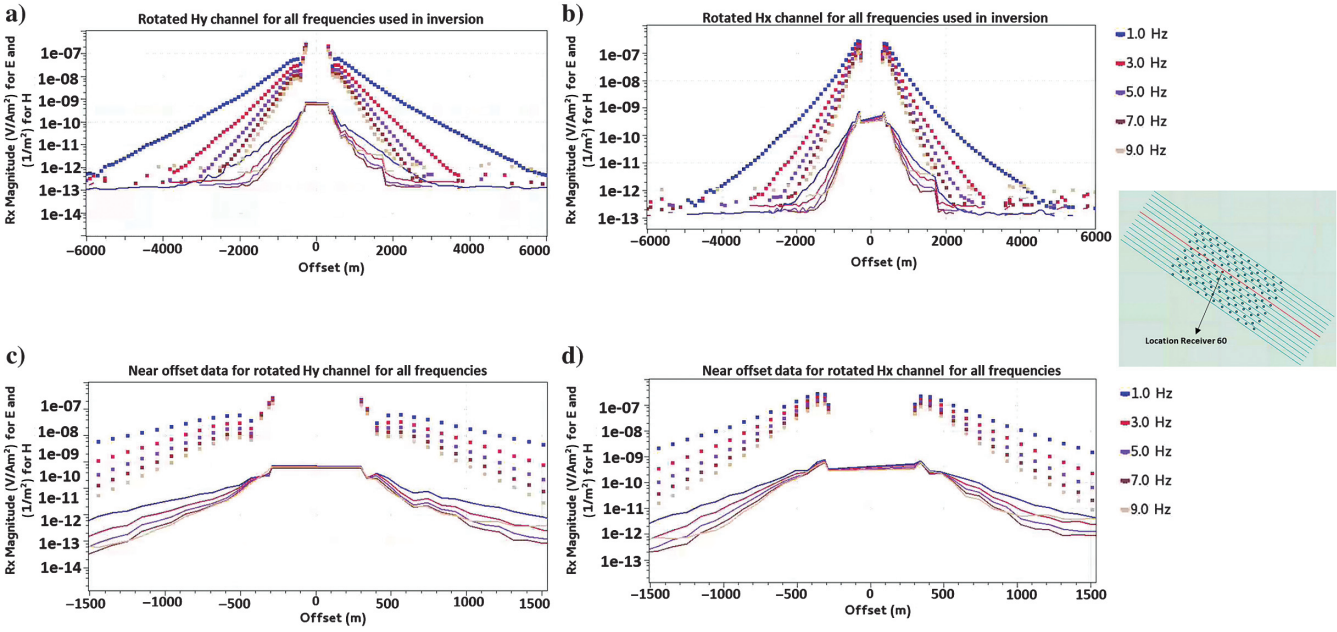

Figure 7. Example CSEM data for receiver 01Rx60a shown for all frequencies. (Top) Magnitude versus offset (MvO) of rotated (a) Hy channel and (b) Hx channel for all of the offsets used in the inversion. (Bottom) MvO for all frequencies of rotated (a) Hy channel and (b) Hx channel for the near-offset data. This is shown to indicate the first sample recorded. Location of the receiver in the survey grid shown in the image beside the plots. The colored curves indicate the noise floor for each frequency (in the same color). Noise is calculated based on the fast Fourier transform in a noise band slightly apart from the transmittal frequency. The signal gets stronger as the source moves closer to the receiver (at zero offset); hence, the noise appears to be higher here.

more random (noise) (Figure 9 and Appendix A). However, magnetic channel-based inversion looked smooth and more consistent with events observed on seismic. This effect was further confirmed in synthetic modeling and inversion tests performed on a theoretical model (Appendix A). A possible reason for this may be due to the presence of small-scale surface anomalies that are known to distort electromagnetic fields (Singer, 1990). The distortion is mainly caused by the electric field because it is sensitive to current flow and the charge distribution generated due to the current flow, through these surface anomalies. This additional charge component creates anomalous distortions/artifacts. However, the magnetic field is only sensitive to current flowing through these anomalies (because the charge is zero) and hence are expected to look smoother, and less distorted, than the electric field. Furthermore, magnetic channel-based inversion shows a resistive layer (of approximately 1.7 Ωm) seen at approximately 400 m below the seafloor, which seems to coincide with the BSR level indicating that this could be geologic. This is not evident in the electric channel inversion possibly due to the distortions. Thus, it resulted in the decision not to pursue the electric channel inversion and focus on the magnetic channel inversion instead.

Input parameters used for the magnetic channel 3D inversion are listed in Table 1. Quantitative assessment of inversion quality is done by evaluating the inversion data misfit. The data misfit is a measure of data fit to the acquired/observed data, and it is defined by significant misfit function, which is the difference between the observed data (acquired data) and the synthetic data (simulated from the inverted model) divided by the relative uncertainty. Relative uncertainty, which depends on the source system used for acquisition and the water depth of the survey area, is estimated to be 3.7% for this survey. The estimate is based on the linear error propagation analysis as detailed by Mittet and Morten (2012). The inversion converged in 25 iterations to reach the estimated relative uncertainty (i.e., rms misfit of ≈ 1), as exemplified by the convergence curve for the rms misfit (Figure 10a) for all receivers including all data channels, frequencies, and offsets used in the inversion (Figure 10b). The magnitude of the significant misfit for all receivers near towline Tx005, for all offsets, is shown in Figure 10c. Plots are shown here for two (1 and 7 Hz) of the five frequencies as an example, to highlight the convergence from iteration 0 (the start model data fit) to iteration 25 (the final model data fit). A significant misfit for the final model could be seen in green (i.e., significant misfit ≪3) for most of the data, and it is considered as a good data fit. Inverted vertical and horizontal resistivity models are displayed in a cross-sectional view, and the map view and 3D view are shown in Figure 11.

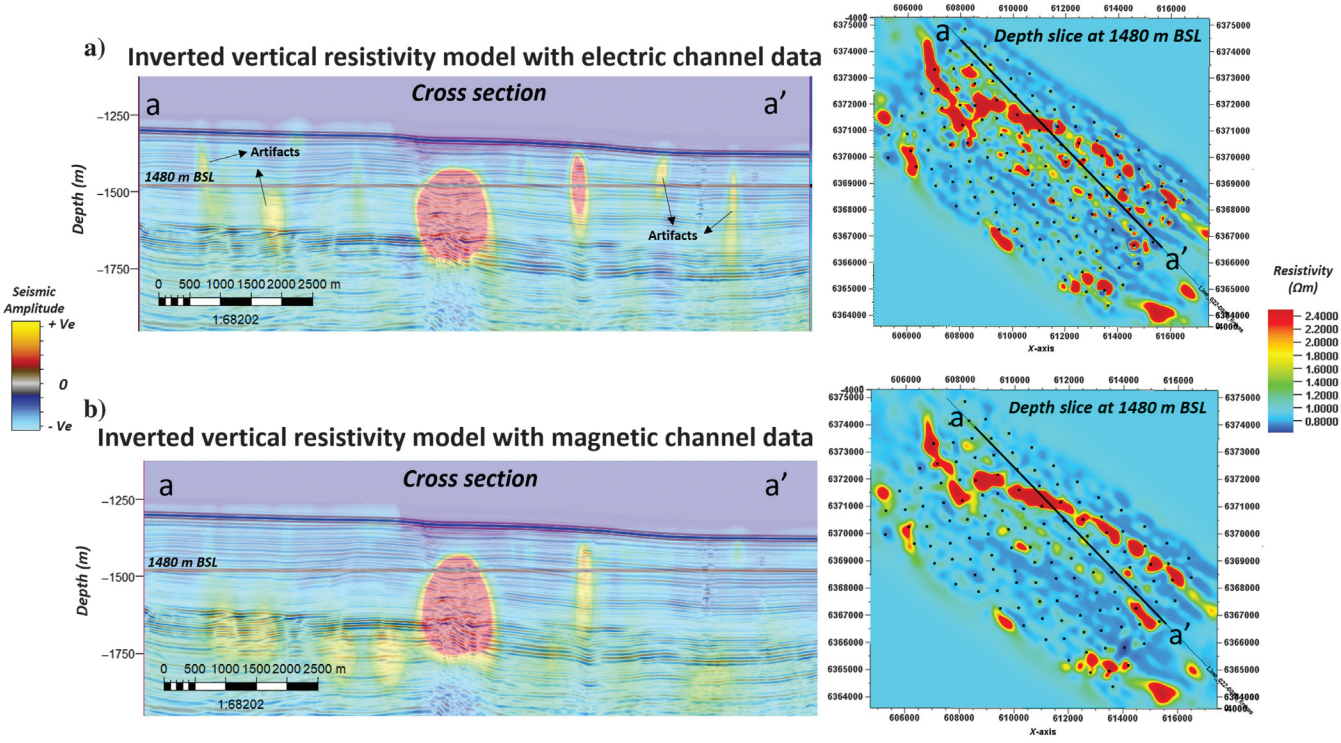

Figure 9. Comparison between electric and magnetic channel inversions. (a) Cross section showing the inverted resistivity model using electric channel data, corendered with seismic. Resistivity artifacts that do not correlate with seismic events are indicated. The depth slice from the inverted vertical model shown on the right indicates several resistivity artifacts suggesting a poorer reconstruction of the subsurface resistivity. (b) Inverted vertical resistivity model using magnetic channel data, corendered with the seismic cross section showing a better correlation between the resistivity anomalies and the seismic events. The depth slice on the right shows a better reconstruction of the subsurface resistivity.

Joint interpretation of CSEM, seismic, and multibeam data

A priori data such as 2D seismic, multibeam backscatter, and piston core data are correlated against the CSEM vertical average resistivity map. An average resistivity map is generated from the 3D CSEM vertical resistivity volume, by integrating the resistivity over a known depth interval (0–360 m below the seabed). The depth interval is chosen such that it encapsulates the entire resistive anomaly. The resultant map provides an average resistivity value and the lateral/areal extent of the resistivity anomalies imaged in that interval. In addition to average resistivity maps the inverted resistivity volumes can be used to generate resistivity anisotropy cubes (Rv/Rh), update cubes (final-initial Rv), and anomalous vertical resistivity (Rv-background Rv) (e.g., Gabrielsen et al., 2013). Figure 12 shows the average vertical resistivity map along with faults mapped on the seabed and multibeam backscatter data. The background resistivity ranges from 0.8 to 1.5 Ωm. There are clearly defined high resistive (>2.6 Ωm) elongated anomalies striking approximately northwest–southeast (Figure 12). Anomalous resistivities seen here are in the same range as noted by Weitemeyer et al. (2011) and Schwalenberg et al. (2010a) in their respective hydrate studies. The anomalies are associated with positive relief features identified on the multibeam data and interpreted from shallow seismic as fault zones extending to the seafloor (Figure 12a). The resistivity varies along the strike of these features, being, particularly strong (4–9 Ωm) in areas with strong backscatter on the multibeam data (Figure 12b).

The resistivity anomalies clearly match with high backscatter patches within pockmarks (Figure 13a) suggesting that the observed anomalies are linked to specific geologic features related to shallow gas migrations, such as authigenic carbonates, gas hydrates (Miller et al., 2015), and chemosynthesis-based communities on the seafloor (Giongo et al., 2016). Along the faults, however, one can identify several locations where a resistivity anomaly does not coincide with a backscatter response (Figure 13b). Conversely, some backscatter does not coincide with high resistive anomalies (Figure 13c). The plausible explanation for the former is that the resistive response is related to hydrocarbons that are supposed to seep to the seafloor and create the backscatter anomaly but are trapped in the subsurface, perhaps by an impermeable gas hydrate plug or other low-permeability zone. This explanation is supported by high seismic amplitudes at the same location, with gas blanking effects beneath (Figure 13b). In cases in which there is no resistivity anomaly (Figure 13c), a plausible interpretation would be that the backscatter response being caused by hydrocarbons migrating upward along the fault without being trapped in the subsurface. The residual fluid has a low saturation gas enough to be seen on seismic but not enough to create a resistive anomaly on CSEM. A second interpretation may be that hydrocarbons migrated along the fault in the past during sufficient time to form chemosynthesis-based communities and authigenic carbonates on the seafloor, which generate strong backscatter, but have ceased to migrate for a long enough period to leave only residual fluid with no resistive anomaly.

There are several other locations in the area where one can identify chimneys related to fluid flow on acoustic data. When superimposed over 3D CSEM data, one can distinguish between a chimney that possibly has fluid trapped within and a chimney that seems to have let all the gas seep toward the seafloor (Figure 14).

The resistivity volume was also compared with piston core information at three locations (Figure 15). No significant resistivity accumulation was seen in the CSEM result at locations A and B, which confirms

Table 1. Final 3D inversion data input and parameterization.

Input receiver data	Parameters		
Field components	Magnetic (Hx, Hy)		
Frequencies and data offset range	Frequency (Hz)	Inner offset limit* (m)	Outer offset limit (m)
	1	1500	6000
	3	1500	3600
	5	1300	3300
	7	1200	2800
	9	1200	2300
Data/noise masking	Data with a signal-to-noise ratio less value of approximately $1e^{-13}$ $1/m^2$ for inline and azimuth data are masked out and excluded from the inversion. The $1/m^2$ unit corresponds to the magnetic field intensity (H fields) scaled by the source dipole moment.		

*Data less than the inner offset limit (i.e., 250 m source receiver offset until the inner offset limit) has not been included in the inversion. The direct field in the seawater dominates the response in these very short offsets which are difficult to model.

the low resistivity logged on the piston bore. Location C has a strong resistivity anomaly in CSEM data, and the same was observed in the piston core resistivity log measurement.

Gas hydrate saturation estimates

The empirical Archie's equation (shown in equation 1) (Archie, 1942), which is meant for pure sands (assuming there is no clay in the system) is used to derive saturation from the resistivity volume:

$$S_{gh} = 1 - \left[\frac{aR_w\varnothing^{-m}}{Rt}\right]^{1/n}, \quad (1)$$

where S_{gh} is the gas hydrate saturation, a is Archie's coefficient, m is the cementation factor, n is the saturation exponent, $\varnothing$ is the porosity, Rw is the interstitial water resistivity, and Rt is the bulk resistivity of the subsurface.

To calculate saturation from a CSEM-derived resistivity volume, we assume $a = 1$, $m = 2.5$, and $n = 2.0$

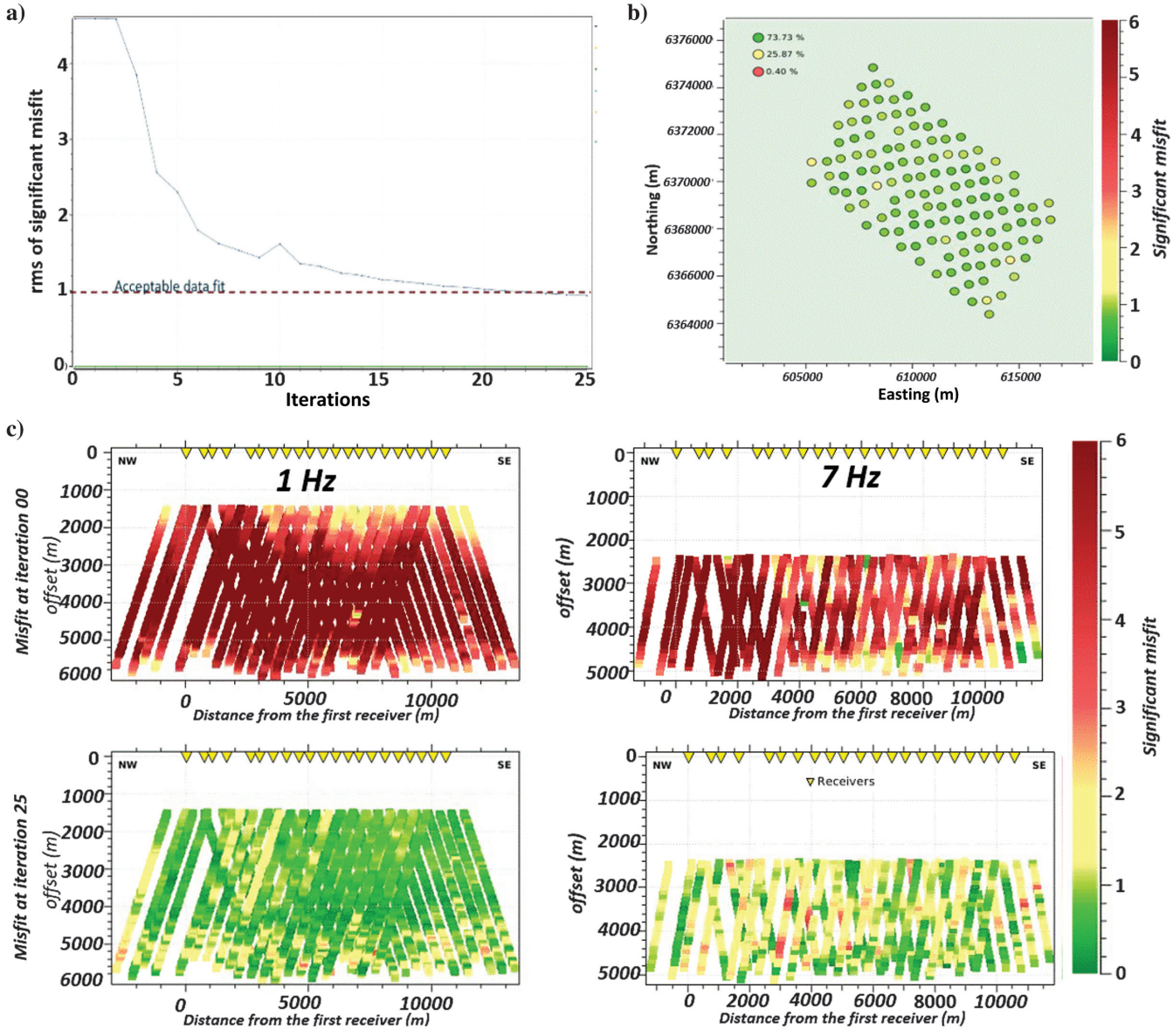

Figure 10. Inversion quality control plots. (a) Convergence curve showing rms of significant misfit for all input data, i.e., magnetic field channels of inline and broadside data. The data converged to a value slightly less than 1, indicating that the relative uncertainty value used is slightly higher and could be reduced. At iteration 10, the inversion chooses an inaccurate local minimum that leads to a higher misfit than the previous iteration. In iteration 11, it finds a better solution. (b) Significant misfit shown per receiver for all frequencies, offsets at the final iteration. The legend shows that 73.73% of the data have a good data fit shown in green, 25.87% of the data have medium or acceptable misfit shown in yellow, and 0.4% of the data have poor misfit shown in red. (c) Magnitude of data residuals for a line of receivers for source towline Tx005 for all offsets for the 1 Hz (left) and 7 Hz (right) frequencies at iteration 0 (top row) and the final iteration 25 (bottom row). Due to the longer skin depth and penetration, the lower frequency (1 Hz) has longer offset (≈6000 m) before it reached the noise floor compared to the higher frequency (7 Hz at ≈5000 m). The same color is used for significant misfit plots in (b and c).

values, which are in line with what is suggested in the literature (e.g., Shankar and Riedel, 2011; Schwalenberg et al., 2017; Cook and Waite, 2018). We assume a constant porosity of 55% suitable for mud sediments at approximately 250 m below the seafloor (Mondol et al., 2007). Resistivity data logged on the piston bore (Figure 15) indicated near-surface resistivity of approximately 0.2 Ωm (Figure 15). We believe that this sediment section should be dominated by brine; thus, the resistivity logged here should be close to *Rw*. Furthermore, we assume that the sediments in the gas hydrate stability zone are unconsolidated with a uniform *Rw*; thus, we apply a constant *Rw* of 0.2 Ωm. Assumptions made here need to be cross verified against wells, which are not available in this study. The term *Rt* in equation 1 is the bulk subsurface resistivity from the inverted CSEM vertical resistivity volume.

Figure 16 shows the S_{gh} volume derived from the CSEM results. Resistivity anomalies seen in the vertical resistivity volume are seen to have saturation varying

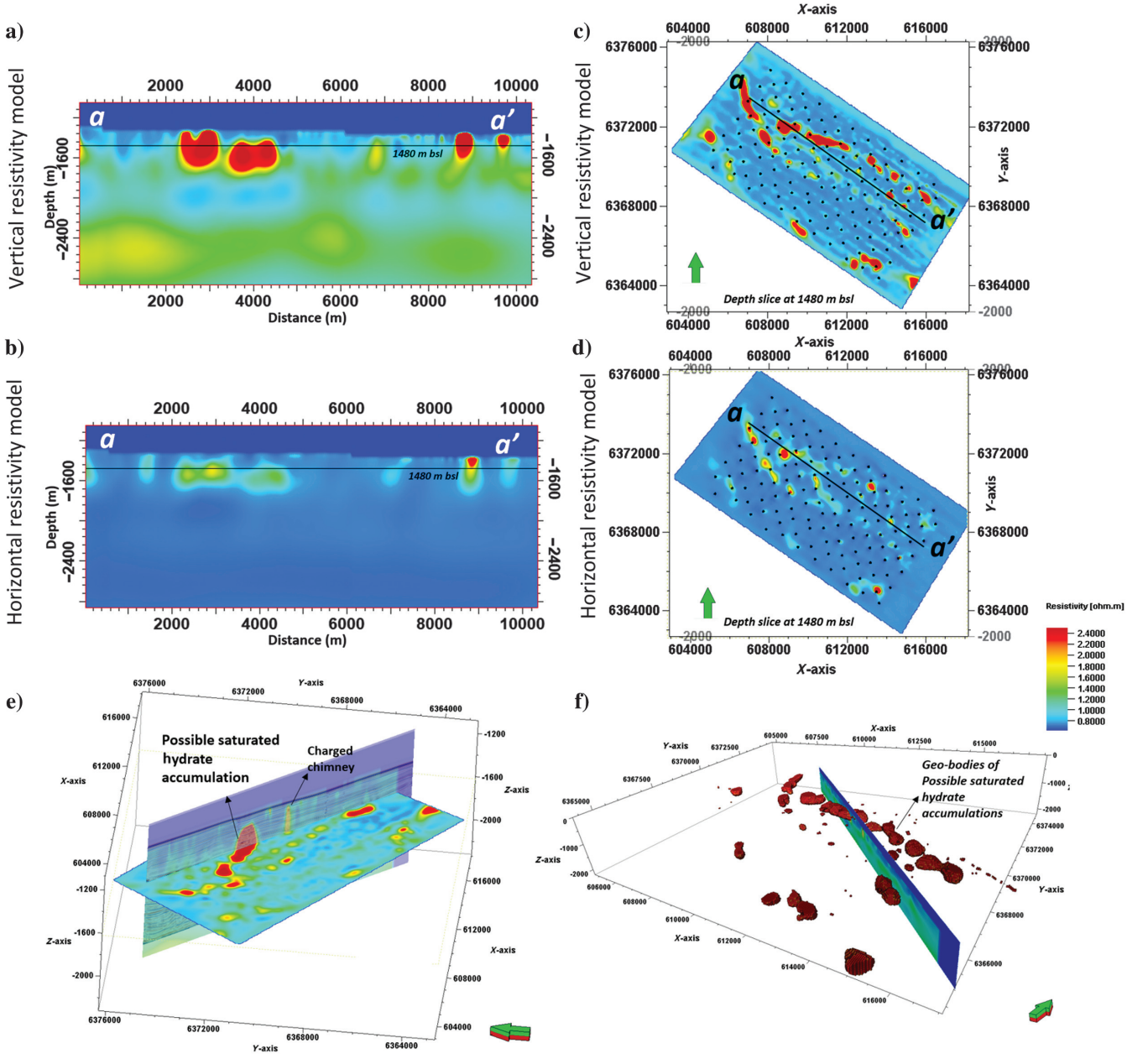

Figure 11. Final model from the CSEM 3D inversion. (a and b) The cross sections of inverted vertical and horizontal resistivity models, respectively, along towline Tx005. CSEM is seen to have sensitivity up to approximately 2500 m below sea level; hence, the model is cropped up to this extent. (c and d) Depth slices of the inverted vertical and horizontal resistivity models, respectively, at 1480 m below sea level. The black dots indicate the receiver grid, and the black line indicates the location of the cross section shown on the left panel. (c) The 3D visualization of a depth section (at 1560 m BSL) from the CSEM vertical resistivity volume with a 2D seismic section indicating possible hydrate accumulations. (d) Anomalous resistivity geobodies (3D volume showing resistivities >2 ohm) that could be the saturated hydrate accumulation shown along with the 2D seismic line for reference.

between 30% and 70%. Resistive anomalies within faults have saturations of approximately 60%, and the gas chimney (shown in Figure 14) has a saturation of approximately 40%. Low saturation values (below 25%) should not be interpreted because the associated resistivities are very close to background resistivities and targets with such low resistivity contrasts are beyond CSEM sensitivity.

These saturation values are highly dependent on the assumptions that are made, and to estimate more meaningful and robust gas hydrate saturation values, one would need to

1) Get a better understanding of saturation coefficients based on well logs from within the study area as done by Shankar and Riedel (2011).

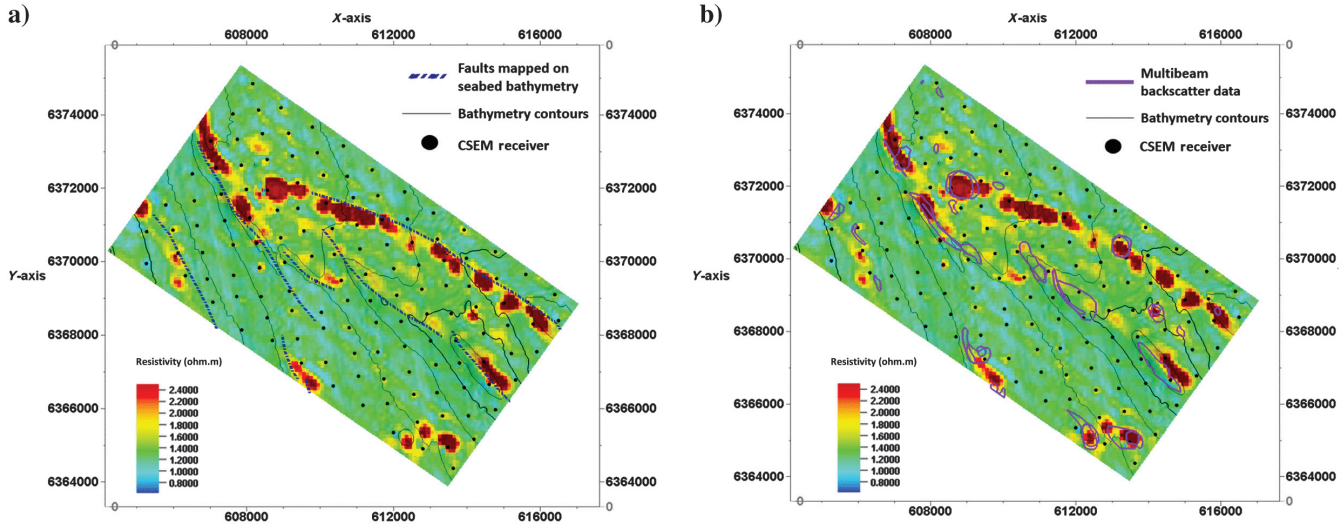

Figure 12. (a) Average vertical resistivity map of the subsurface (resistivity averaged between from 0 to 360 m below water bottom) draped on the seafloor horizon. Faults mapped at the seafloor and isobath lines are shown for reference. (b) The same average map showing the location of the anomalous regions interpreted on the multibeam echo sounder backscatter data (overlain as the purple polygons).

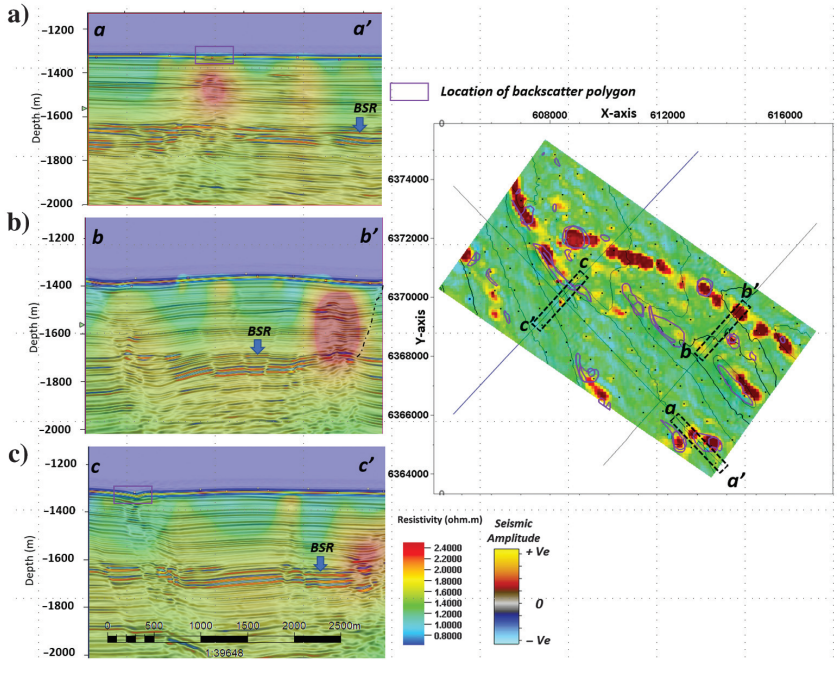

Figure 13. Superimposition of 2D seismic data on the same cross section extracted from the CSEM vertical inversion result shown in the left. The black lines shown on the map in the right indicate the location of the 2D seismic lines, and the dotted rectangles indicate the location of the part of the seismic cross section shown in the left. The average vertical resistivity map (averaged between 0 and 360 m below the water bottom) shown in the right is imprinted on the seabed horizon showing the seabed contour lines (in black). The contour lines are shown only to indicate the seabed variation and how resistivity anomalies align with these variations. The purple polygons are multibeam backscatter data. Seismic cross sections in the left showing (a) a good correlation between the resistivity and backscatter data (the location of backscatter data is indicated with a purple rectangle on the cross section), (b) a resistive response but no backscatter response at the seafloor, and (c) backscatter response (indicated with the purple rectangle on cross section) but no resistivity response in CSEM. The vertical scale is in true vertical depth below sea level. Smoothness algorithm in which the cells in the 3D model are rendered by squared distance weighting has been applied to the CSEM cube.

2) Include realistic porosity trends as done by Schwalenberg et al. (2017) on the Hikurangi Margin, New Zealand, instead of the constant value used in the current study.
3) Understand the volume of clay and use a modified version of Archie's equation such as Simandoux (1963) equation, Fertl (1975) equation, or the Poupon and Leveaux (1971) (Indonesia) equations to account for the volume of clay.
4) The CSEM inversion is known to underestimate resistivity in the resultant model. In the presence of a well log providing a true resistivity value of the target hydrate and 3D seismic providing the true structure of a hydrate-bearing sediment, one can build a true geologic model and perform synthetic modeling and inversion studies. By evaluating target resistivity in the true model and resistivity in the resultant synthetic inversion model, one can quantify this

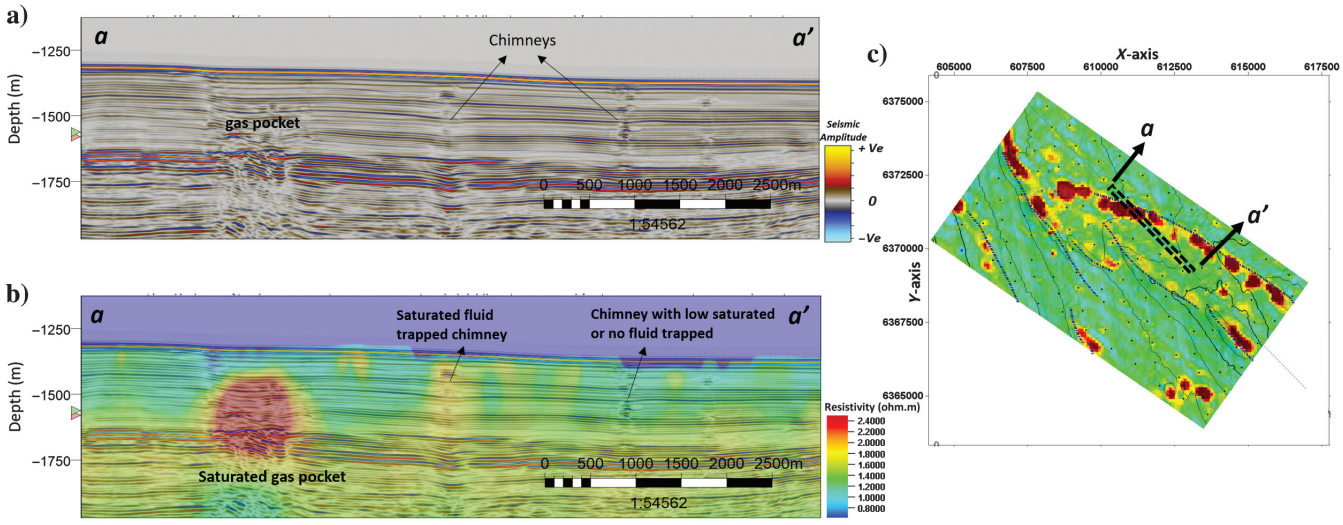

Figure 14. (a) Interpretation based on seismic alone and (b) interpretation based on seismic superimposed with CSEM vertical resistivity volume. Location of seismic cross section shown in the black dashed rectangle over the average vertical resistivity map. (c) The dashed blue lines on the map indicate faults mapped on the seafloor, and black lines indicate isobathy lines. With seismic and CSEM, one can differentiate between resistive/saturated fluid trapped chimney and a low-resistivity/low-saturation chimney. The seismic seabed and the CSEM seabed do not match here because the EM resistivity volume is corendered (covisualized) against a depth-converted 2D seismic profile. The seabed in the CSEM model is built based on bathymetry measurements done while acquiring the data (based on source navigation). Along the CSEM towlines there is a good control on the bathymetry, and between towlines the bathymetry is interpolated. The seismic 2D lines are not along the CSEM towlines, and the interpolation causes the mismatch. A smoothness algorithm in which the cells in the 3D model are rendered by squared distance weighting has been applied to the CSEM cube.

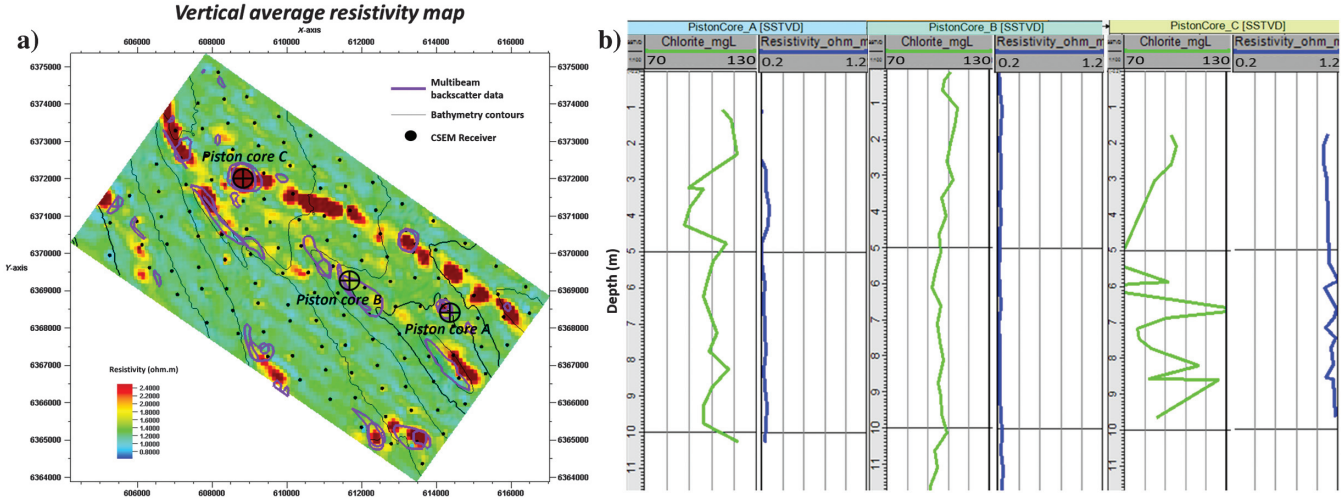

Figure 15. (a) Location of piston cores shown on the CSEM average resistivity map. (b) Log data acquired while piston coring. The logs include chloride content and resistivity measurements. The location at piston core C has high resistivities in the CSEM data set and the log data.

underestimation factor and apply this to the real inversion result to overcome this underestimation.

Nonetheless, saturation derived from CSEM is useful because it is derived from an independent nonseismic measurement (CSEM) and can be used to evaluate and cross check saturation models derived using traditional seismic-based methods.

Benefits and limitations of CSEM for hydrate mapping

We would like to address some of the limitations of this method of collecting, processing, and inverting data. The method discussed here is capable of detecting resistive (saturated) hydrates that are within the CSEM sensitivity (as indicated in the sensitivity plot in Figure 3) and grid spacing limitations. Hydrate accumulations that are (laterally) smaller and are closer to the seabed will be beyond CSEM detection limits due to reasons such as the source setup used, near-offset data (that could contain information about these hydrates) that are not being used in the inversion, and grid spacing economics (i.e., a denser grid with crossline towing would help but will increase the cost of acquisition). However, if this is a sizable target, this method should be able to detect the entire hydrate feature even if it is at the seabed as exemplified in Figure 17 due to the available broadside data.

It is important to stress that CSEM data can provide an additional constraint for improved interpretation. For a conventional reservoir at very shallow subsurface depths comparable to the Pelotas Basin study area, Granli et al. (2017) illustrate how an integrated approach involving geology-driven scenario testing and joint interpretation can be used to the extent to which fluid contacts can be predicted to within a few meters prior to drilling the appraisal boreholes.

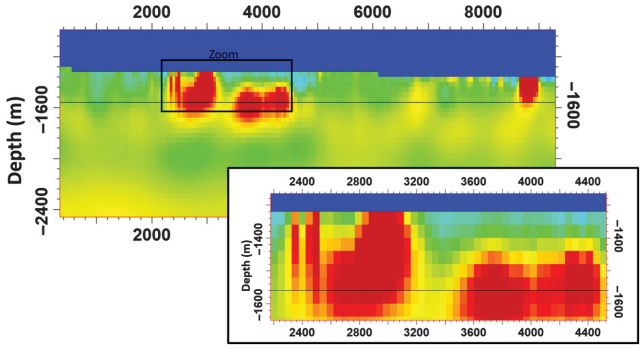

Figure 17. Magnified image of a cross section of the CSEM inversion result shown (Figure 11) without the smoothness algorithm applied. The anomaly extends from the first cell below the water bottom indicating that CSEM can detect shallow anomalies if the dimensions of the anomaly fall within the CSEM sensitivity range.

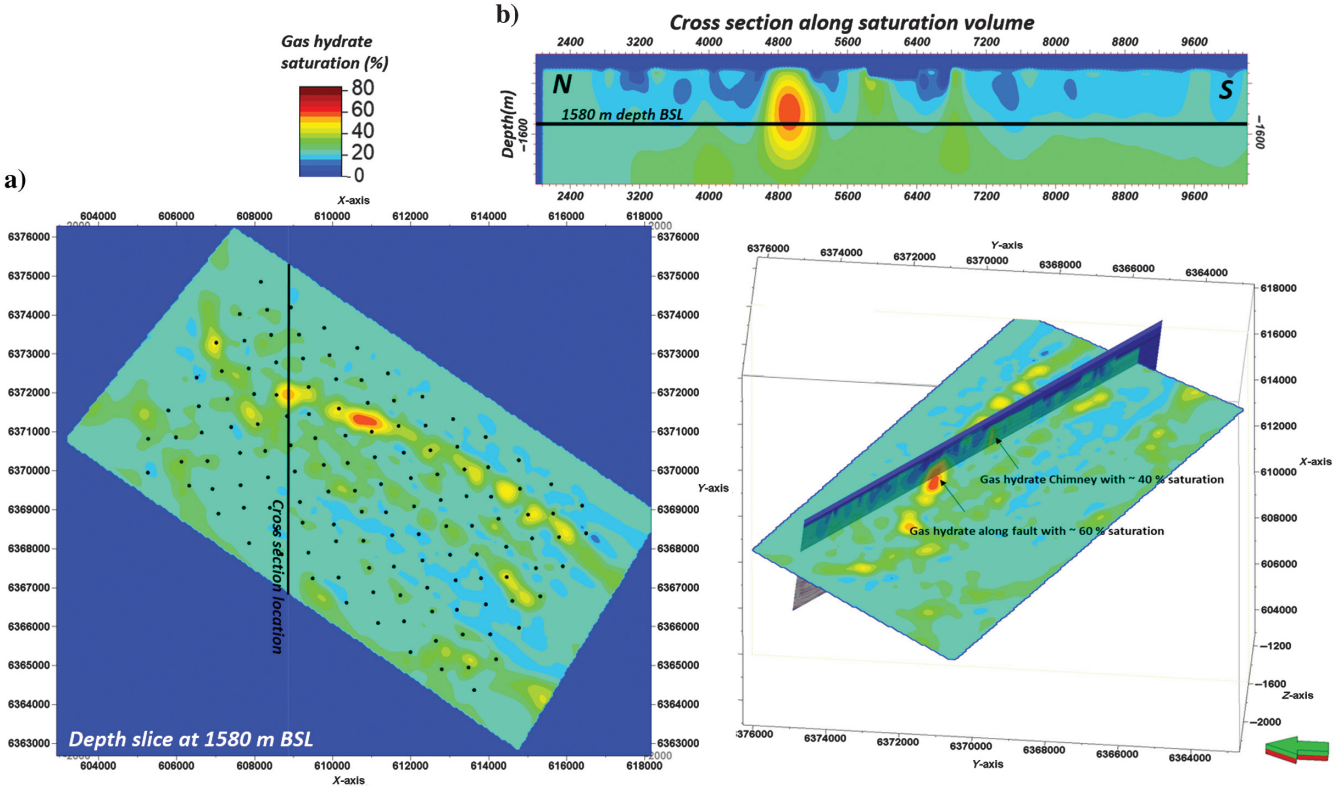

Figure 16. Saturation volume derived from the resistivity volume. (a) Depth slice of the saturation volume at 1580 m below mean sea level (BMSL) and (b) a random cross section from the saturation volume. (c) 3D view showing a cross section of the 2D seismic corendered with the saturation volume with the depth slice of the saturation volume at 1580 m BMSL.

In a gas hydrate province, localized increases in resistivity can be related to several factors that reduce the amount of electrically conductive brine, either by porosity reduction or the substitution of brine by a significant amount of nonconductive pore-filling material such as hydrocarbons or gas hydrates (Senger et al., 2017). Increased resistivity can be related to a significant increase in gas saturation within the free gas zone beneath the BSR, high-saturation hydrates within the hydrate stability zone, or the presence of significant amounts of low-porosity carbonates. A proper depositional understanding is essential to rule out such possible antimodels.

Distinguishing resistivity effects near the BSR level is notoriously difficult, given that the free gas contribution beneath the BSR and gas hydrate contributions above the BSR will contribute to the overall formation resistivity; however, detailed synthetic inversions using geology-driven and scenario-based start models could quantify the relative contributions of these two potential resistors. Thus, CSEM is more suited for spatially differentiating the high-saturation "sweet spots" within the gas hydrate stability zone and any high-saturation pockets of free gas immediately beneath the BSR.

Conclusions

We have presented results of a hydrate-specific 3D CSEM study from the gas hydrate province of the Pelotas Basin. We conclude that (1) 3D CSEM inversion results provide valuable information concerning the location and extent of saturated gas hydrates/free gas in the subsurface. (2) Gas hydrates/free gas has variable saturation, and the saturated hydrates are not extensive wherever there is BSR as previously assumed. (3) Correlating these results with multibeam backscatter data offers a new insight to the gas trapping and migration mechanism in the subsurface.

Furthermore, this information could be used (1) to accurately reestimate gas volumes present in the hydrate-associated system, either for gas hydrate commercialization and/or for methane-based climate change assessment and (2) in drilling operations, for the placement of exploration wells away from gas hydrate-related hazards.

Acknowledgments

The authors thank PETROBRAS for sponsoring this research and for the permission to publish this paper, the IHS Global Inc. Educational/Academic Grant Program for the use of the Kingdom Software. We also thank EMGS for allowing us to publish this paper. Finally, we sincerely appreciate the constructive comments from the editors of the journal, D. Colombo, and two anonymous reviewers.

Data and materials availability

Data can be provided for research upon request.

Appendix A

Synthetic modeling and inversion study

Synthetic modeling and inversion tests shown here aim to address the following topics:

1) Generate an optimum grid design to map shallow resistors.
2) Evaluate inversion results run using E channel data and H channel data.

For this synthetic study, resistivity models (vertical and horizontal models) are built with representative nonhydrate sediment resistivities (background resistivities) based on the real inversion result. Three realistic targets are imprinted on the background resistivity model. The first target represents a hydrate formed in a sand channel (slump), the second target is hydrate accumulated along the fault, and the third target is hydrate in a vertical chimney. Gas hydrate targets have resistivity of 6 Ωm. Figure A-1 shows the model with the background and targets imprinted (called the true model).

Synthetic data are simulated using this true model with a grid configuration per the objective. Channels, frequencies, and offsets generated in the synthetic data set are identical to the real data. The 3D inversion is run using this synthetic data simulated from the true model as the input data to the inversion. The start model used in the inversion is a simple half-space model (with a single resistivity value in the subsurface). Inversions converged to an acceptable misfit for all of the inversion jobs.

Objective 1: Grid design test

All of the grid design inversion tests shown here are using magnetic H channel data. Figure A-2 shows the resultant vertical resistivity models of the different grid geometries tested.

A 1×1 km receiver inline and crossline spacing and with the source towed on the receiver line is generally used in conventional hydrocarbon exploration in which the target is expected to have a minimum areal extent of approximately 1–2 km^2 and is buried at shallow to intermediate depths (300–1000 m below the mudline). When such a design is used for hydrates, one can see from Figure A-2a that it is too coarse to be able to capture all of the targets (especially targets 1 and 3). Added to this resistive survey footprints in the first cell below the water bottom make it difficult to interpret these results.

A $1\ km \times 500\ m$ inline and crossline staggered receiver grid with the source towed on the receivers is a finer grid that is suitable to image smaller targets compared to the 1×1 km grid. One can see in Figure A-2b that this grid is able to capture the three targets with a good lateral positioning (seen on the depth slice). However, because the source is towed over the receiver, one can see resistive survey footprints in the first cell below the water bottom, which could be a concern during interpretation of the results.

With the same $1\ km \times 500\ m$ inline and crossline receiver grid, when the source is towed in between

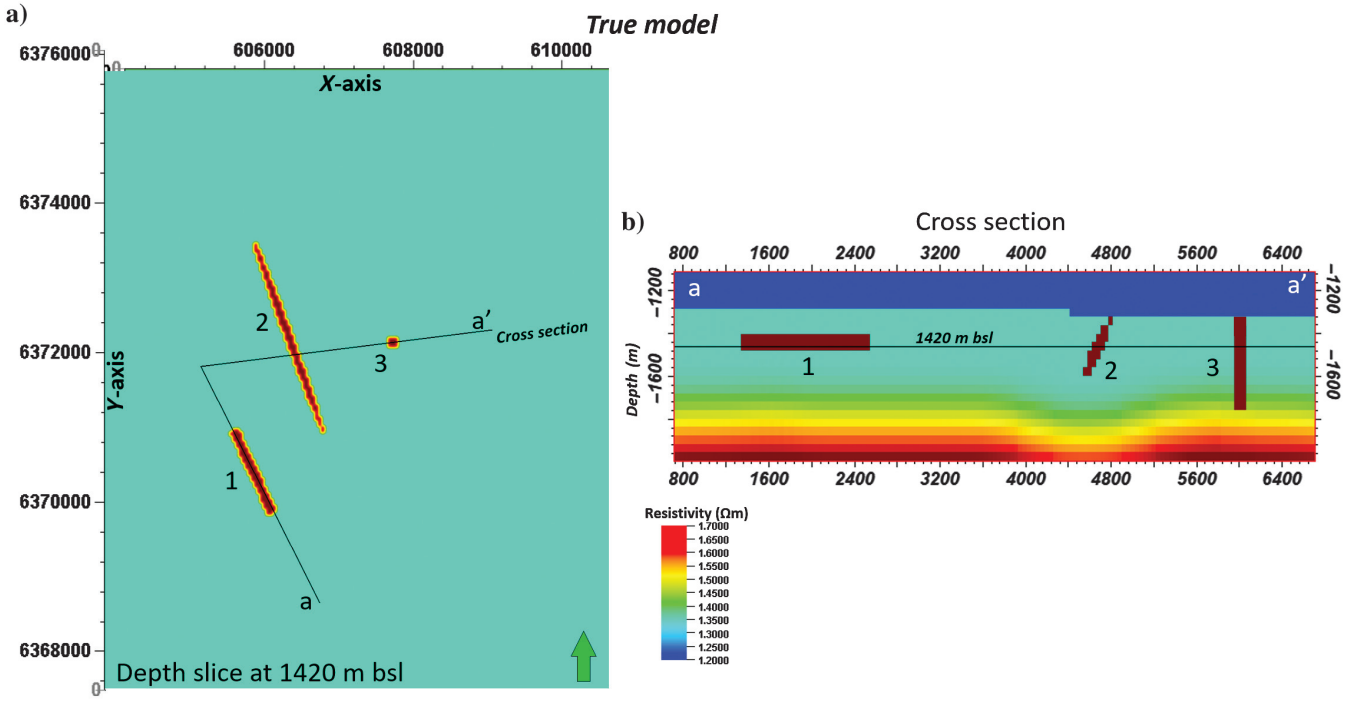

Figure A-1. True model used for synthetic inversion studies. (a) Depth slice of the true model with three targets indicating a channel (1), a fault (2), and a vertical chimney (3). (b) Cross section showing all three targets. The location of the depth slice is indicated with a black line.

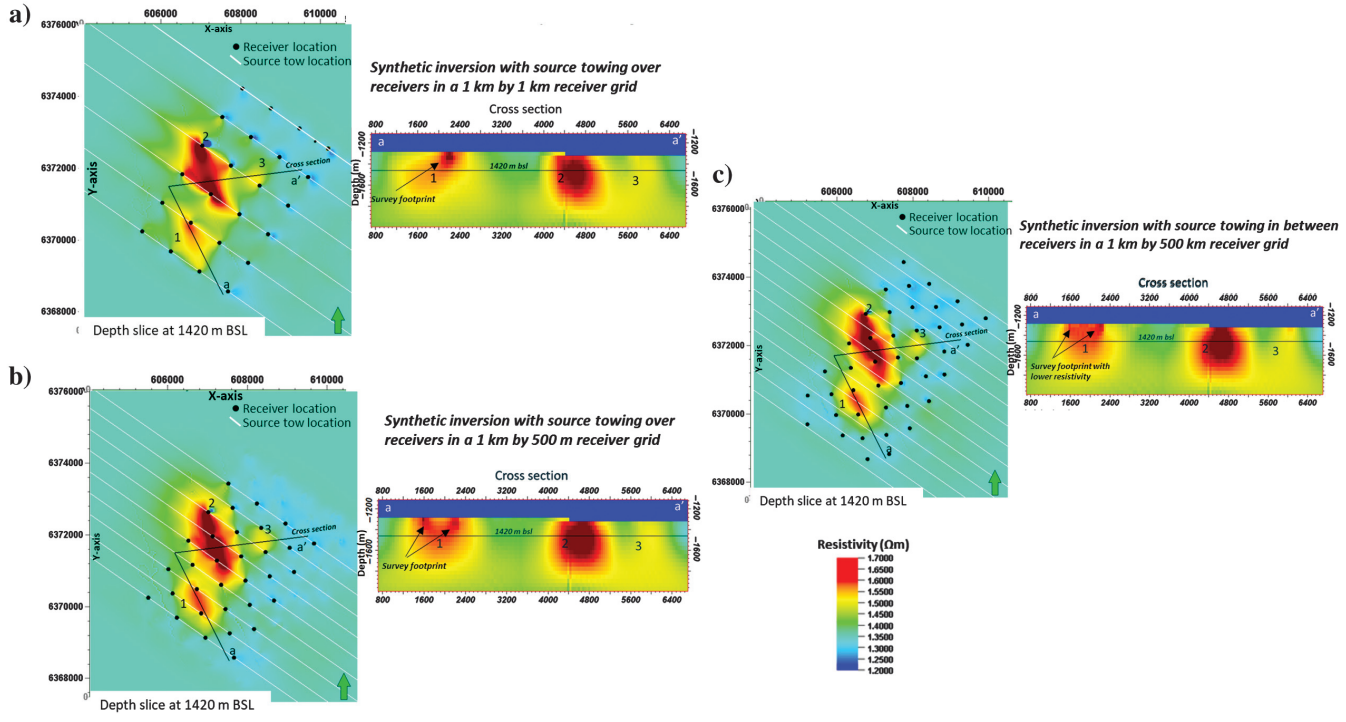

Figure A-2. (a) Synthetic inversion run using a 1 × 1 km receiver spacing with the source towed on the receiver line. (b) Synthetic inversion run using a 1 km × 500 m receiver spacing with the source towed on the receiver line. (c) Synthetic inversion run using a 1 km × 500 m receiver spacing with the source towed in between the receiver line. Depth slice and cross section of resultant models with all three targets indicating a channel (1), a fault (2), and a vertical chimney (3). The location of the cross section is indicated on the depth slice with the black line. The location of the depth slice is indicated on the cross section with the black line.

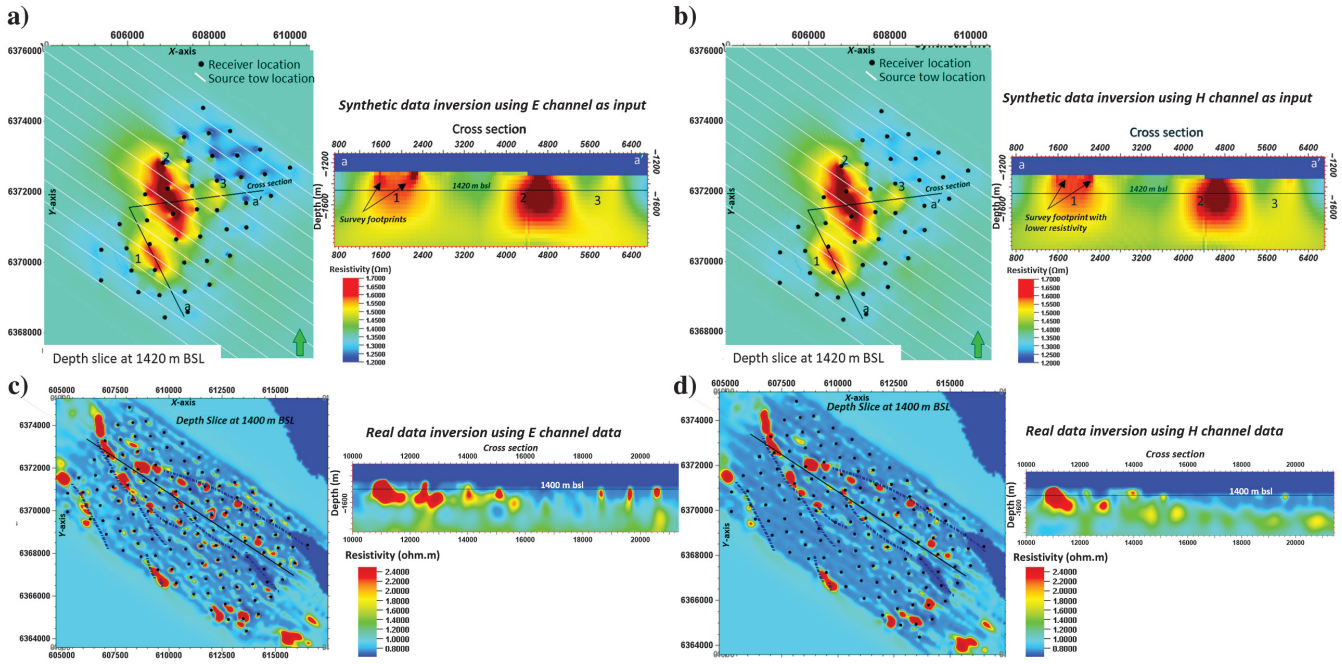

Figure A-3. (a) Synthetic inversion run using the electric channel showing conductive and resistive artifacts associated with the receivers that distort the shape of targets imaged. (b) Synthetic inversion run using magnetic channels showing a more smoother inversion result with fewer artifacts. Depth slice and cross section of the inverted synthetic model with three targets indicating a channel (1), a fault (2), and a vertical chimney (3). The location of the cross section is indicated on the depth slice with black line. The location of the depth slice is indicated on the cross section with a black line. (c) Depth slice and cross section of the real data inversion run using the electric channel showing artifacts similar to what is seen on synthetic data inversion and (d) magnetic channel showing a smooth result similar to what is seen on synthetic data inversion.

the receiver lines, the survey footprint impact is seen to reduce to some extent (Figure A-2c). All of the targets are imaged comparatively well.

Objective 2: Electric channel versus magnetic channel inversion

Using the survey grid shown in Figure A-2c, one inversion was run using E channel data as input and another inversion with H channel data as input. All other inversion parameters are identical. Figure A-3 shows the results of E channel data inversion and H channel data inversion.

E channel data inversion (Figure A-3a) images all three targets; however, the resultant model indicates conductive and resistive artifacts in the model similar to the real data inversion result run with the E channel data (Figure A-3c).

The H channel data inversion (Figure A-3b) resultant model is smoother in comparison to E channel data inversion and is similar to the real data inversion result run with the H channel data (Figure A-3d).

These results support the argument stated in the paper.

References

Archie, G. E., 1942, The electrical resistivity log as an aid in determining some reservoir characteristics: Petroleum Technology, **1422**, 54–62.

Asmus, H. E., and P. R. Baisch, 1983, Geological evolution of the Brazilian continental margin: Episodes, **1983**, 3–9.

Attias, E., K. Weitemeyer, T. A. Minshull, A. I. Best, M. Sinha, M. Jegen-Kulcsar, S. Hölz, and C. Berndt, 2016, Controlled-source electromagnetic and seismic delineation of subseafloor fluid flow structures in a gas hydrate province, offshore Norway: Geophysical Journal International, **206**, 1093–1110, doi: 10.1093/gji/ggw188.

Boswell, R., and T. S. Collett, 2011, Current perspectives on gas hydrate resources: Energy Environmental Science, **4**, 1206–1215, doi: 10.1039/C0EE00203H.

Castillo, L. L. A., T. de S. Kazmierczak, and F. Chemale Jr., 2009, Rio grande cone tectono-stratigraphic model — Brazil: Seismic sequences: Earth Sciences Research Journal, **13**, 42–53.

Collett, T. S., A. H. Johnson, C. C. Knapp, and R. Boswell, 2009, Natural gas hydrates: A review, *in* T. Collett, A. Johnson, C. Knapp, and R. Boswell, eds., Natural gas hydrates energy resource potential and associated geologic hazards: AAPG Memoir 89, 146–219.

Constable, S., 2010, Ten years of marine CSEM for hydrocarbon exploration: Geophysics, **75**, no. 5, 75A67–75A81, doi: 10.1190/1.3483451.

Constable, S., P. K. Kannberg, and K. Weitemeyer, 2016, Vulcan: A deep-towed CSEM receiver: Geochemistry, Geophysics, Geosystems, **17**, 1042–1064, doi: 10.1002/2015GC006174.

Cook, A. E., and W. F. Waite, 2018, Archie's saturation exponent for natural gas hydrate in coarse-grained reservoirs: Journal of Geophysical Research: Solid Earth, **123**, 2069–2089.

Dickens, G. R., 2011, Down the rabbit hole: Toward appropriate discussion of methane release from gas hydrate systems during the Paleocene-Eocene thermal maximum and other past hyperthermal events: Climate of the Past, **7**, 831–846, doi: 10.5194/cp-7-831-2011.

Du Frane, W. L., L. A. Stern, S. Constable, K. A. Weitemeyer, M. M. Smith, and J. J. Roberts, 2015, Electrical properties of methane hydrate + sediment mixtures: Journal of Geophysical Research: Solid Earth, **120**, 4773–4783, doi: 10.1002/2015JB011940.

Du Frane, W. L., L. A. Stern, K. A. Weitemeyer, S. Constable, J. C. Pinkston, and J. J. Roberts, 2011, Electrical properties of polycrystalline methane hydrate: Geophysical Research Letters, **38**, L09313, doi: https://doi.org/10.1029/2011GL047243.

Edwards, N., 2005, Marine controlled source electromagnetics: Principles, methodologies, future commercial applications: Surveys in Geophysics, **26**, 675–700, doi: 10.1007/s10712-005-1830-3.

Eidesmo, T., S. Ellingsrud, L. MacGregor, S. Constable, M. Sinha, S. Johansen, F. Kong, and H. Westerdahl, 2002, Sea bed logging (SBL), a new method for remote and direct identification of hydrocarbon filled layers in deepwater areas: First Break, **20**, 144–152.

Fanavoll, S., P. Gabrielsen, and S. Ellingsrud, 2014, CSEM as a tool for better exploration decisions: Case studies from the Barents Sea, Norwegian Continental Shelf: Interpretation, **2**, no. 3, SH55–SH66, doi: 10.1190/INT-2013-0171.1.

Fertl, W. H., 1975, Shaly sand analysis in development wells: Presented at the SPWLA 16th Annual Logging Symposium.

Fontana, R. L., 1989, Evidências geofísicas da presença de hidratos de gás na Bacia de Pelotas — Brasil: 1o Cong. Soc. Bras. Geofísica 1.

Fontana, R. L., and A. Mussumeci, 1994, Hydrates offshore Brazil: Annals of the New York Academy of Sciences: International Conference on Natural Gas Hydrates 715, 106–113.

Freij-Ayoub, R., C. Tan, B. Clennell, B. Tohidi, and J. Yang, 2007, A wellbore stability model for hydrate bearing sediments: Journal of Petroleum Science and Engineering, **57**, 209–220, doi: 10.1016/j.petrol.2005.10.011.

Gabrielsen, P. T., P. Abrahamson, M. Panzner, S. Fanavoll, and S. Ellingsrud, 2013, Exploring frontier areas using 2D seismic and 3D CSEM data, as exemplified by multiclient data over the Skrugard and Havis discoveries in the Barents Sea: First Break, **31**, 63–71.

Gehrmann, R. A., K. Schwalenberg, M. Riedel, G. D. Spence, V. Spieß, and S. E. Dosso, 2016, Bayesian inversion of marine controlled source electromagnetic data offshore Vancouver Island, Canada: Geophysical Journal International, **204**, 21–38, doi: 10.1093/gji/ggv437.

Giongo, A., T. Haag, T. L. L. Simão, R. Medina-Silva, R. P. Utz Laura, M. R. Bogo, S. L. Bonatto, P. M. Zamberlan, A. H. Augustin, R. V. Lourega, L. F. Rodrigues, G. F. Sbrissa, R. O. Kowsmann, A. F. M. Freire, D. J. Miller, A. R. Viana, J. M. M. Ketzer, and E. Eizirik, 2016, Discovery of a chemosynthesis-based community in the western South Atlantic Ocean: Deep Sea Research Part I: Oceanographic Research Papers, **112**, 45–56.

Goswami, B. K., K. A. Weitemeyer, S. Bünz, T. A. Minshull, G. K. Westbrook, S. Ker, and M. C. Sinha, 2017, Variations in pockmark composition at the Vestnesa Ridge: Insights from marine controlled source electromagnetic and seismic data: Geochemistry, Geophysics, Geosystems, **18**, 1111–1125, doi: 10.1002/2016GC006700.

Goswami, B. K., K. A. Weitemeyer, T. A. Minshull, M. C. Sinha, G. K. Westbrook, A. Chabert, T. J. Henstock, and S. Ker, 2015, A joint electromagnetic and seismic study of an active pockmark within the hydrate stability field at the Vestnesa Ridge, West Svalbard margin: Journal of Geophysical Research: Solid Earth, **120**, 6797–6822.

Granli, J. R., H. H. Veire, P. T. Gabrielsen, and J. P. Morten, 2017, Maturing broadband 3D CSEM for improved reservoir property prediction in the Realgrunnen Group at Wisting, Barents Sea: 87th Annual International Meeting, SEG, Expanded Abstracts, 2205–2209, doi: 10.1190/segam2017-17727091.1.

Grauls, D., 2001, Gas hydrates: Importance and applications in petroleum exploration: Marine and Petroleum Geology, **18**, 519–523, doi: 10.1016/S0264-8172(00)00075-1.

Hesthammer, J., A. Stefatos, M. Boulaenko, S. Fanavoll, and J. Danielsen, 2010, CSEM performance in light of well results: The Leading Edge, **29**, 34–41, doi: 10.1190/1.3284051.

Hunter, S. J., D. S. Goldobin, A. M. Haywood, A. Ridgwell, and J. G. Rees, 2013, Sensitivity of the global submarine hydrate inventory to scenarios of future climate change: Earth and Planetary Science Letters, **367**, 105–115, doi: 10.1016/j.epsl.2013.02.017.

Hyndman, R. D., and G. Spence, 1992, A seismic study of methane hydrate marine bottom simulating reflectors: Journal of Geophysical Research, **97**, 6683–6698, doi: 10.1029/92JB00234.

Kannberg, P., and S. Constable, 2017, Web reference, https://marineemlab.ucsd.edu/Projects/GoMHydrate2017/index.html, accessed 17 June 2019.

Kennett, J. P., K. G. Cannariato, I. L. Hendy, and R. J. Behl, 2003, Methane hydrates in quaternary climate change: The clathrate gun hypothesis: American Geophysical Union.

Ketzer, M., D. Praeg, M. A. G. Pivel, A. Augustin, L. F. Rodrigues, A. Viana, and J. A. Cupertino, 2019, Gas seeps at the edge of the gas hydrate stability zone on Brazil's continental margin: Geosciences, **9**, 193–11, doi: 10.3390/geosciences9050193.

Kvenvolden, K. A., 1993, Gas hydrates — Geological perspective and global change: Reviews of Geophysics, **31**, 173–187, doi: 10.1029/93RG00268.

MacGregor, L., and J. Tomlinson, 2014, Marine controlled-source electromagnetic methods in the hydrocarbon industry: A tutorial on method and practice: Interpretation, **2**, no. 3, SH13–SH32, doi: 10.1190/INT-2013-0163.1.

Martins, L. R., U. Melo, A. M. C. França, C. I. Santana, and I. R. Martins, 1972, Distribuiçao faciologica da margem continental sul riograndense: 26th Congresso Brasileiro de Geologia, Expanded Abstracts, 115–132.

McConnell, D. R., Z. Zhang, and R. Boswell, 2012, Review of progress in evaluating gas hydrate drilling hazards: Marine and Petroleum Geology, **34**, 209–223, doi: 10.1016/j.marpetgeo.2012.02.010.

Medina-Silva, R., R. R. Oliviera, F. J. Trindade, L. G. A. Borges, T. L. L. Simao, A. H. Augustin, F. P. Valdez, M. J. Constant, C. L. Simundi, E. Eizirik, C. Groposo, D. J. Miller, P. R. da Silva, A. R. Viana, J. M. M. Ketzer, and A. Giongo, 2017, Microbiota associated with tubes of Escarpia sp. from cold seeps in the southwestern Atlantic Ocean constitutes a community distinct from that of surrounding marine sediment and water: Antonie van Leeuwenhoek - International Journal of General and Molecular Microbiology, **111**, 533–550, doi: 10.1007/s10482-017-0975-7.

Miller, D. J., J. M. M. Ketzer, A. R. Viana, R. O. Kowsmann, A. F. M. Freire, S. G. Oreiro, A. H. Augustin, R. V. Lourega, L. F. Rodrigues, R. Heemann, A. G. Preisler, C. X. Machado, and G. F. Sbrissa, 2015, Natural gas hydrates in the Rio Grande Cone (Brazil): A new province in the western South Atlantic: Marine and Petroleum Geology, **67**, 187–196, doi: 10.1016/j.marpetgeo.2015.05.012.

Mittet, R., and J. P. Morten, 2012, Detection and imaging sensitivity of the marine CSEM method: Geophysics, **77**, no. 6, E411–E425, doi: 10.1190/geo2012-0016.1.

Mondol, N. H., K. Bjørlykke, J. Jahren, and K. Høeg, 2007, Experimental mechanical compaction of claymineral aggregates — Changes in physical properties of mudstones during burial: Marine and Petroleum Geology, **24**, 289–311, doi: 10.1016/j.marpetgeo.2007.03.006.

Morten, J. P., and A. K. Bjørke, 2010, Fast-track marine CSEM processing and 3D inversion: 72nd Annual International Conference and Exhibition, EAGE, Extended Abstracts, doi: 10.3997/2214-4609.201400660.

OEdigital, 2014, Web reference, https://www.oedigital.com/news/454352-ofg-completes-japanese-csem-survey, accessed 17 June 2019.

Oliveira, S., O. Vilhena, and E. da Costa, 2010, Time-frequency spectral signature of Pelotas Basin deep water gas hydrates system: Marine Geophysical Research, **31**, 89–97, doi: 10.1007/s11001-010-9085-x.

Pinero, E., M. Marquardt, C. Hensen, M. Haeckel, and K. Wallmann, 2013, Estimation of the global inventory of methane hydrates in marine sediments using transfer functions: Biogeosciences, **10**, 959–975, doi: 10.5194/bg-10-959-2013.

Poupon, A., and J. Leveaux, 1971, Evaluation of water saturation in Shaly Formations (abs): Society of Professional Well Log Analysists Annual logging Symposium, **12**, O1–O2.

Rodrigues, L. F., J. M. Ketzer, R. V. Lourega, A. H. Augustin, G. Sbrissa, D. J. Miller, R. Heemann, A. R. Viana, A. F. M. Freire, and S. Morad, 2017, The influence of methane fluxes on the sulfate/methane interface in sediments from the Rio Grande cone gas hydrate Province, southern Brazil: Brazilian Journal of Geology, **47**, 369–381, doi: 10.1590/2317-4889201720170027.

Sad, A. R. E., D. P. Silveira, and M. A. P. Machado, 1997, Hidratos de ga s marinhos: A mega-ocorrencia da Bacia de Pelotas/Brasil: 5th International Congress of the Brazilian Geophysical Society, Extended Abstracts, 71–74.

Sad, A. R. E., D. P. Silveira, M. A. P. Machado, S. R. P. Silva, and R. R. Maciel, 1998, Marine gas hydrates evidence along the Brazilian coast: AAPG International Conference and Exhibition, Abstracts.

Saunders, M., S. Bowman, and L. Geiger, 2013, The Pelotas Basin oil province North-West revealed: GEO ExPro, **4**, 38–40.

Schwalenberg, K., M. Haeckel, J. Poort, and M. Jegen, 2010a, Evaluation of gas hydrate deposits in an active seep area using marine controlled source electromagnetics: Results from Opouawe Bank, Hikurangi Margin, New Zealand: Marine Geology, **272**, 79–88, doi: 10.1016/j.margeo.2009.07.006.

Schwalenberg, K., D. Rippe, S. Koch, and C. Scholl, 2017, Marine-controlled source electromagnetic study of methane seeps and gas hydrates at Opouawe Bank, Hikurangi Margin, New Zealand: Journal of Geophysical Research: Solid Earth, **122**, 3334–3350.

Schwalenberg, K., W. Wood, I. Pecher, L. Hamdan, S. Henrys, M. Jegen, and R. Coffin, 2010b, Preliminary interpretation of electromagnetic, heat flow, seismic, and geochemical data for gas hydrate distribution across the Porangahau Ridge, New Zealand: Marine Geology, **272**, 89–98, doi: 10.1016/j.margeo.2009.10.024.

Senger, K., T. Birchall, S. Ohm, K. Ogata, and S. Olaussen, 2017, Review of geological controls on resistivity in uplifted basins: Insights from the Norwegian Barents shelf: AAPG International Conference and Exhibition, 10.

Shankar, U., and M. Riedel, 2011, Gas hydrate saturation in the Krishna-Godavari basin from P-wave velocity and electrical resistivity logs: Marine and Petroleum Geology, **28**, 1768–1778, doi: 10.1016/j.marpetgeo.2010.09.008.

Shantsev, D. V, and F. A. Maao, 2014, Rigorous interpolation near tilted interfaces in 3-D finite-difference EM modelling: Geophysical Journal International, **200**, 745–757, doi: 10.1093/gji/ggu429.

Silveira, D. P., and M. A. P. Machado, 2004, Bacias sedimentares brasileiras: Bacia de Pelotas: Phoenix, Série Bacias Sedimentares.

Simandoux, P., 1963, Dielectric measurements in porous media and application to shaly formation: Revue del'Institut Francais du Petrole, Supplementary Issue, 193–215, (Translated text in SPWLA Reprint Volume Shaly Sand, July 1982).

Singer, B., 1990, Correction of distortions of magnetotelluric fields: Limits of validity of the static approach: Surveys in Geophysics, **13**, 309–340, doi: 10.1007/BF01903482.

Sloan, E. D., and C. Koh, 2007, Clathrate hydrates of natural gases: CRC Press Taylor and Francis Group 119, 9–625.

Spangenberg, E., and J. Kulenkampff, 2006, Influence of methane hydrate content on electrical sediment properties: Geophysical Research Letters, **33**, L24315, doi: 10.1029/2006GL028188.

Weitemeyer, K., and S. Constable, 2010, Mapping shallow geology and gas hydrate with marine CSEM surveys: First Break, **28**, 97–102.

Weitemeyer, K. A., S. Constable, K. Key, and J. Behrens, 2006, First results from a marine controlled-source electromagnetic survey to detect gas hydrates offshore Oregon: Geophysical Research Letters, **33**, doi: 10.1029/2005GL024896.

Weitemeyer, K. A., S. Constable, and A. M. Tréhu, 2011, A marine electromagnetic survey to detect gas hydrate at Hydrate Ridge, Oregon: Geophysical Journal International, **187**, 45–62, doi: 10.1111/j.1365-246X.2011.05105.x.

Worthington, P. F., 1993, The uses and abuses of the Archie equations. 1: The formation factor-porosity relationship: Journal of Applied Geophysics, **30**, 215–228, doi: 10.1016/0926-9851(93)90028-W.

Zach, J. J., F. Roth, and H. Yuan, 2008, Data preprocessing and starting model preparation for 3D inversion of marine CSEM surveys: 70th Annual International Conference and Exhibition, EAGE, Extended Abstracts, doi: 10.3997/2214-4609.20147712.

Zhu, C., R. H. Byrd, and J. Nocedal, 1997, L-BFGS-B: Algorithm 778: L-BFGS-B, FORTRAN routines for large scale bound constrained optimization: ACM Transactions on Mathematical Software, **23**, 550–560, doi: 10.1145/279232.279236.

Biographies and photographs of the authors are not available.